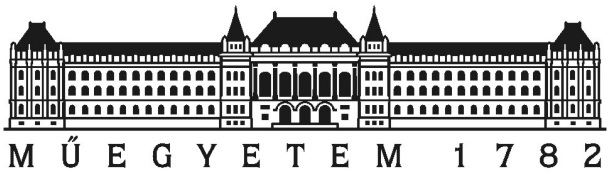


Diploma Thesis

# Building MRI probehead for a 7T Bruker NMR device

Ádám Ottó Kettinger

Supervisor: Dr. Dávid Légrády
Associate Professor
BME Institute of Nuclear Techniques
Department of Nuclear Techniques

**Budapest University of Technology and Economics**

**2014**

MŰEGYETEM 1782

# Diplomamunka feladat a Fizikus mesterképzési (MSc) szak hallgatói számára

| | | | |
|---|---|---|---|
| A hallgató neve: | **Kettinger Ádám Ottó** | szakiránya: | **orvosi fizika** |
| A diplomamunkát gondozó (a záróvizsgát szervező) tanszék: | | | **Nukleáris Technika Tanszék** |

| | | | |
|---|---|---|---|
| A diplomamunka készítésének helye: | **Budapesti Műszaki és Gazdaságtudományi Egyetem** | | |
| A témavezető neve: | **Légrády Dávid** | A konzulens neve: (külső témavezető esetén kijelölt tanszéki munkatárs) | |
| – munkahelye: | **NTI** | | |
| – beosztása: | **egyetemi docens** | – beosztása: | |
| – e-mail címe: | **legrady@reak.bme.hu** | – e-mail címe: | |

| | | |
|---|---|---|
| A diplomamunka címe: | **MRI mérőfej építése 7T Bruker NMR mágneshez** | azonosítója: **DM-2013-94** |

A téma rövid leírása, a megoldandó legfontosabb feladatok felsorolása:

Napjaink legdinamikusabban fejlődő orvosi képalkotó modalitása a Mágneses Rezonancia Képalkotás (MRI), térnyerése szembetűnő a hagyományos modalitások (CT, PET, SPECT) kiegészítéseként, de olykor akár helyettesítéseként is. Az MRI készülék több, egymástól lényegileg eltérő információgyűjtő mérési szekvenciával működhet, melyek in vivo képesek szerkezeti (anatómiai) információkon túl funkcionális jellemzőket is vizsgálni. A Fizika Tanszéken rendelkezésre áll egy Bruker AVANCE DRX 300MHz spektrométer és egy 7T terű szupravezető mágnes, illetve szintén rendelkezésre áll megfelelő gradiens vezérlő. A hallgató feladata - Rádiófrekvenciás mérőfej készítése a mérési paraméterek mellett a maximális mintaméretre is optimalizálva - a tomográfiás képalkotáshoz szükséges gradiens tekercsek tervezése és kivitelezése - a legalább 1D képalkotásra alkalmas rendszer jel/zaj viszonyainak jellemzése mérések és számítások segítségével

| | |
|---|---|
| A feladat kiadásának időpontja: | **2013. február 11.** |

| | |
|---|---|
| Témavezető vagy tanszéki konzulens aláírása: | A diplomamunka témakiírását jóváhagyom (tanszékvezető aláírása): |

# Önállósági nyilatkozat

Alulírott Kettinger Ádám Ottó, a Budapesti Műszaki és Gazdaságtudományi Egyetem fizikus MSc szakos hallgatója kijelentem, hogy ezt a diplomamunkát meg nem engedett segédeszközök nélkül, önállóan, a témavezető irányításával készítettem, és csak a megadott forrásokat használtam fel. Minden olyan részt, melyet szó szerint, vagy azonos értelemben, de átfogalmazva más forrásból vettem, a forrás megadásával jelöltem.

Budapest, 2014. június 1.

_____

Kettinger Ádám Ottó

# Köszönetnyilvánítás

Ezúton szeretnék köszönetet mondani mindazoknak, akik útmutatásukkal, türelmükkel, hozzáértésükkel segítették ennek a dolgozatnak a létrejöttét. Köszönöm Légrády Dávidnak, hogy lehetővé tette a projektben való részvételemet és vállalta a témám vezetését. Úgy gondolom, az általa felkínált lehetőség és az elvégzett munka nagyban elősegítette, hogy egy napon a mágneses rezonanciához értő szakember váljon belőlem.

Köszönöm Simon Ferencnek a munkához elengedhetetlenül szükséges hozzáférést az NMR berendezéshez és a laborban található egyéb eszközökhöz, illetve a rengeteg hasznos szakmai tanácsot, amit tőle kaptam. Köszönöm a Fizika Tanszék műhelyének, hogy a szükséges alkatrészeket mindig pontosan és gyorsan elkészítették; az ő segítségük nélkül már a legegyszerűbb mérések is szinte kivitelezhetetlenné váltak volna.

Köszönöm Dávid Szabolcsnak, hogy felkeltette bennem a kezdeti érdeklődést az MRI iránt, és megmutatta az ebben a technikában rejlő óriási lehetőségeket.

Köszönöm Gyebnár Gyulának, hogy munkatársként együtt dolgozhattunk a projekt során. Jelfeldolgozásban és mérési eljárásokban végzett munkája lehetővé tette, hogy a megépített mérőfej egy tényleges képalkotó eszközzé váljon. Úgy gondolom, hogy a közös eszmecserék, a felmerülő problémákon való együtt gondolkodás mindkettőnk szakmai fejlődését nagyban elősegítette.

Végezetül köszönöm Szüleimnek, Barátaimnak és Páromnak, hogy a munka hátteréhez szükséges családi és emberi hátteret megteremtették és megteremtik folyamatosan. Az ő türelmük és támogatásuk adta meg az alapot nem csupán ennek a dolgozatnak, de egész tanulmányaimnak és fejlődésemnek.

# Contents

# 1. Introduction

In the last few decades medical imaging techniques have shown stupendous development as they evolved from cumbersome experimental devices to the high precision tomographic instruments as we know them today. Among the variety of imaging modalities magnetic resonance imaging have attracted a particularly strong interest in medical science since its invention as it has an outstanding soft tissue contrast, and furthermore, this is the only whole-body imaging technique that avoids the use of ionizing radiation.

Recently the progression in MRI hardware and the usage of special acquisition methods made this modality capable not just to show detailed anatomy of the patient, but also to provide a wide range of information like neural activity in fMRI or white matter fiber structure in dMRI. Since the invention of these technologies, magnetic resonance imaging became a comprehensive tool for researchers from broad areas such as physicists, neurobiologists and pharmaceutical companies.

In this work we aimed to upgrade an NMR device with imaging capabilities by designing and building a small MRI probehead, and also by implementing some of the commonly used image acquisition and reconstruction methods on a machine originally designed for spectroscopy. I worked in this twin thesis in collaboration with an other MSc student called Gyula Gyebnár. The division of effort was roughly the following: I was responsible for the design, construction and testing of hardware elements like radiofrequency coils and gradient coils, while Gyula's part was the gradient driving circuits, the implementation of imaging algorithms and the image reconstruction. Although this collaboration caused unavoidable overlaps in some work sections, these points are always clearly marked in this thesis.

In the beginning of this paper I will walk through the fundamental physics of magnetic resonance followed by the principles of imaging. Thereafter stands the two main chapters of my work: the radiofrequency system and the gradient system. In both parts I investigate the theoretical background of the topic first, then I present my workflow in details including not just the construction, but also the testing of the built imaging hardware. Finally I will show some of the images acquired by our device and algorithms.

# 2. Theoretical background of magnetic resonance

By the middle of the 1920's the famous experiment performed by W. Gerlach and O. Stern [1] made it clear that the electron has an intrinsic angular momentum referred to as spin. Following this concept, Rabi and his coworkers continued the research on the spin of the proton and its interaction with a magnetic field in the 1930's [2]. With their results given in 1946, Purcell and Bloch succesfully measured the effect of precession of the spins around a magnetic field and also explained the theoretical background of this phenomenon [3, 4]. The contribution of these early results to modern MRI technology is unquestionable: without the understanding of the physics of nuclear magnetic resonance, its application to biomedical imaging would be impossible.

In the following the basic principles of spin precession and excitation is presented followed by the concept of relaxation and spin echo. These processes can be described in two ways: using classical magnetic moments or quantum mechanics. It can be shown that the two approaches lead to equivalent results, i.e. the mean value of the quantum mechanical quantities are the same as come from the classical description [6]. In this thesis the equivalence will be shown solely for the precession in Appendix B, beyond that the classical way is presented because of its far more intuitive and graphic nature. In the following chapters of theoretical background I mostly rely on the book Magnetic Resonance Imaging written by E. Mark Haacke et al. [6], which is one of the most comprehensive works on this topic in my opinion, and on the lectures of Kálmán Nagy titled Magnetic Resonance and its Clinical Applications at Budapest University of Technology and Economics.

## 2.1 Fundamental interaction of spins with magnetic field - precession

In the classical way the first step of investigating the interaction of a spin with external magnetic field is to derive the classical connection between angular momentum and magnetic moment. The simplest model for this is the circulating point charge as shown in Figure 2.1.

For the magnetic moment, we will use the commonly known classical expression [7]:

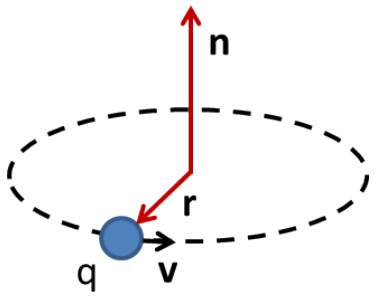


Figure 2.1: Circulating point charge with charge q and velocity $\mathbf{v}$

$$\boldsymbol{\mu} = \frac{1}{2}\int \mathbf{r} \times \mathbf{J}(\mathbf{r})\mathrm{d}^3\mathrm{r} = \frac{1}{2}q\mathbf{r} \times \mathbf{v} = \frac{1}{2}qvr\mathbf{n} \tag{2.1}$$

Whilst for the angular momentum

$$\mathbf{I} = m\mathbf{r} \times \mathbf{v} = mvr\mathbf{n} \tag{2.2}$$

In (2.1) and (2.2) $\boldsymbol{\mu}$ stands for the magnetic moment, $\mathbf{J}(\mathbf{r})$ for the electric current density, $\mathbf{n}$ for the normal vector of the circulatory plane, and $\mathbf{I}$ for the angular momentum.

If we have not just a single point charge but an extensive rotating body with spatially varying electric charge density $\sigma(\mathbf{r})$ and mass density $\rho(\mathbf{r})$ then the expressions are as follows:

$$\boldsymbol{\mu} = \frac{1}{2}\int \mathbf{r} \times \mathbf{J}(\mathbf{r})\mathrm{d}^3\mathrm{r} = \frac{1}{2}\int \mathbf{r} \times \sigma(\mathbf{r})\mathbf{v}(\mathbf{r})\mathrm{d}^3\mathrm{r} \tag{2.3}$$

$$\mathbf{I} = \int \mathbf{r} \times \rho(\mathbf{r})\mathbf{v}(\mathbf{r})\mathrm{d}^3\mathrm{r} \tag{2.4}$$

From equations (2.3) and (2.4) follows that if we assume our extended body to have mass density and electric charge density to be proportional, which means they vary the same way in space, then the magnetic moment and the angular momentum also become proportional:

$$\boldsymbol{\mu} = \frac{q}{2m}\mathbf{I} = \gamma\mathbf{I} \tag{2.5}$$

Where $\gamma$ is the so-called gyromagnetic ratio which plays vital role in magnetic resonance.

To derive the equation of motion of a spin in external field we will use another two formulas: the connection between angular momentum and torque (the latter denoted by $\mathbf{N}$), and the torque that applies to a magnetic moment in external magnetic field.

$$\frac{\mathrm{d}\mathbf{I}}{\mathrm{d}t} = \mathbf{N} \tag{2.6}$$

$$\mathbf{N} = \boldsymbol{\mu} \times \mathbf{B} \tag{2.7}$$

From equations (2.5), (2.6) and (2.7) we can easily find that the equation of motion for the magnetic moment of a spin in external field is the following:

$$\frac{\mathrm{d}\boldsymbol{\mu}}{\mathrm{d}t} = \gamma\boldsymbol{\mu} \times \mathbf{B} \tag{2.8}$$

(2.8) describes a clockwise precession around the magnetic field as shown in Figure 2.2. The angular frequency of the precession is determined by the product of the magnetic field and the gyromagnetic ratio and is called Larmor frequency:

$$\boldsymbol{\omega}_0 = -\gamma\mathbf{B} \tag{2.9}$$

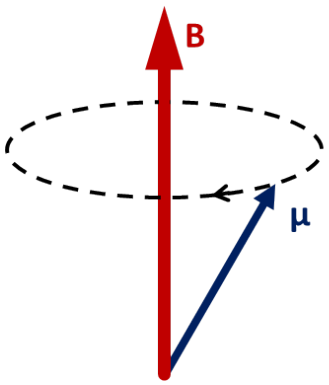


Figure 2.2: Magnetic moment precessing around external magnetic field

From now on without loss of generality we suppose the magnetic field to be parallel with the $z$ axis. With this assumption the solution of (2.8) by components are

$$\mu_x(t) = \mu_x(0)\cos(\omega_0 t) + \mu_y(0)\sin(\omega_0 t) \tag{2.10}$$

$$\mu_y(t) = -\mu_x(0)\sin(\omega_0 t) + \mu_y(0)\cos(\omega_0 t) \tag{2.11}$$

$$\mu_z(t) = \mu_z(0) \tag{2.12}$$

From (2.12) we can see that the $z$ component is constant in time, so we only have to deal with $x$ and $y$ components. We can do so by gathering these two components into a vector that describes the transverse projection of the magnetic moment denoted by $\boldsymbol{\mu}_\perp$:

$$\frac{\mathrm{d}\boldsymbol{\mu}_\perp}{\mathrm{d}t} = \gamma\boldsymbol{\mu}_\perp \times \mathbf{B} \tag{2.13}$$

By using complex formalism, the mathematical description of these components becomes more manageable. Let's make a time dependent complex number from these two with $\mu_x$ and $\mu_y$ stand as the real and the imaginary part respectively, and let's denote it by $\mu_+$. In this way, the magnetic moment can be written as

$$\mu_+(t) = \mu_x(t) + \mathrm{i}\mu_y(t) = \mu_+(0)\mathrm{e}^{-\mathrm{i}\omega_0 t} \tag{2.14}$$

In this way, the two independent components are no more $\mu_x$ and $\mu_y$ but the amplitue and phase of a complex number. It is extremely important to notice that the phase in this representation is not an arbitrary, non-physical parameter like the phase of the wavefunction in basic quantum mechanics, but closely relates to the position of the precessing moment and is of utmost importance in the description of spin motion and magnetic resonance imaging.

## 2.2 Rotating reference frame, RF excitation and resonance

Both in NMR and MRI technology always exists a static magnetic field denoted by $\mathbf{B_0}$, so the Larmor precession caused by this static field is somewhat trivial. Therefore, it would be desireable to eliminate this fundamental precession movement from the mathematical description. In general, this is achieved by introducing a rotating coordinate system [8], or with a more intuitive expression, by "rotating together with the spins".

We will use a coordinate system that rotates with angular frequency $\boldsymbol{\Omega}$. Mathematically the connection between the time derivative of a dynamic vector $\mathbf{b}(t)$ in such a coordinate system and in a static system can be described by the following:

$$\left.\frac{\mathrm{d}\mathbf{b}}{\mathrm{d}t}\right|_{\text{static}} = \left.\frac{\mathrm{d}\mathbf{b}}{\mathrm{d}t}\right|_{\text{rotating}} + \boldsymbol{\Omega} \times \mathbf{b} \tag{2.15}$$

Using (2.15) and (2.8) for the time derivative of the magnetic moment in the static field $\mathbf{B_0}$ we get:

$$\gamma\boldsymbol{\mu} \times \mathbf{B_0} = \left.\frac{\mathrm{d}\boldsymbol{\mu}}{\mathrm{d}t}\right|_{\text{static}} = \left.\frac{\mathrm{d}\boldsymbol{\mu}}{\mathrm{d}t}\right|_{\text{rotating}} + \boldsymbol{\Omega} \times \boldsymbol{\mu} \tag{2.16}$$

From this the time derivative in the rotating system:

$$\left.\frac{\mathrm{d}\boldsymbol{\mu}}{\mathrm{d}t}\right|_{\text{rotating}} = \gamma\boldsymbol{\mu}\times\mathbf{B_0} + \boldsymbol{\mu}\times\boldsymbol{\Omega} = \gamma\boldsymbol{\mu}\times\underbrace{\left(\mathbf{B_0}+\frac{\boldsymbol{\Omega}}{\gamma}\right)}_{\mathbf{B_{eff}}} \tag{2.17}$$

As can be seen from above, the introduction of a coordinate system rotating with angular frequency $\boldsymbol{\Omega}$ is equivalent to the alternation of the static magnetic field by $\frac{\boldsymbol{\Omega}}{\gamma}$. The result is called the effective magnetic field, and it has a concrete physical meaning: in the rotating system the spins seem to move like they were precessing around this effective field $\mathbf{B_{eff}}$. The reader now might see one of the benefits of this description method: if we choose the angular frequency of the rotating system to be equal to the Larmor frequency, that is, if $\boldsymbol{\Omega} = \boldsymbol{\omega_0}$, then in this system the spins remain still, or in other words, the effective magnetic field becomes zero:

$$\left.\frac{\mathrm{d}\boldsymbol{\mu}}{\mathrm{d}t}\right|_{\text{rotating}} = \gamma\boldsymbol{\mu}\times\underbrace{\left(\mathbf{B_0}+\frac{\boldsymbol{\omega_0}}{\gamma}\right)}_{\mathbf{B_{eff}}} = \gamma\boldsymbol{\mu}\times\underbrace{\left(\mathbf{B_0}-\frac{\gamma\mathbf{B_0}}{\gamma}\right)}_{\mathbf{B_{eff}}} = \mathbf{0} \tag{2.18}$$

From now on, unless marked, we will continue the mathematical description in a rotating system.

Next, we will deal with the usual process of manipulating spins: the radiofrequency or RF excitation. First we assume that beyond the static field $\mathbf{B_0}$ we have a linearly polarized magnetic field denoted by $\mathbf{B_1^{lin}}(t)$ oscillating in the plane orthogonal to $\mathbf{B_0}$ (called transverse plane) with an angular frequency $\boldsymbol{\omega}$ and has an amplitude $b_1$. In the static system, this field can be written as

$$\mathbf{B_1^{lin}}(t) = b_1\cos(\omega t)\mathbf{e_x} \tag{2.19}$$

Where $\mathbf{e_x}$ refers to the unit vector at the $x$ direction in the static system. For the rotating system, we will use the notation $\mathbf{e'_x}$ in the same role. For simpler derivation, let us now define the rotating reference frame using the RF frequency $\boldsymbol{\omega}$, meaning $\boldsymbol{\Omega} = \boldsymbol{\omega}$. To write $\mathbf{B_1^{lin}}(t)$ in the rotating system, we first express the unit vectors of the static system with the unit vectors of the rotating system. In other words:

$$\mathbf{e_x} = \mathbf{e'_x}\cos(\omega t) + \mathbf{e'_y}\sin(\omega t) \tag{2.20}$$

$$\mathbf{e_y} = -\mathbf{e'_x}\sin(\omega t) + \mathbf{e'_y}\cos(\omega t) \tag{2.21}$$

$$\mathbf{e_z} = \mathbf{e'_z} \tag{2.22}$$

Using (2.20) and (2.19) we can obtain the form of $\mathbf{B_1^{lin}}(t)$ in the rotating system:

$$\mathbf{B_1^{lin}}(t) = b_1 \cos(\omega t)\big(\mathbf{e'_x}\cos(\omega t) + \mathbf{e'_y}\sin(\omega t)\big) = \frac{1}{2} b_1 \Big(\mathbf{e'_x}\big[1 + \cos(2\omega t)\big] + \mathbf{e'_y}\big[\sin(2\omega t)\big]\Big) \tag{2.23}$$

In (2.23) the effect of the terms with frequency $2\omega$ is averaged out for all times large compared to the RF period. Because of this, the effect of the RF field in the rotating reference can be substituted with its time averaged version:

$$\Big\langle \mathbf{B_1^{lin}}(t) \Big\rangle = \frac{1}{2} b_1 \mathbf{e'_x} \tag{2.24}$$

As can be seen, the linearly polarized field will act as static in the rotating reference. Here we notice that the effect of a circularly polarized RF field would be almost the same, the only difference is that the factor $\frac{1}{2}$ would be missing.

Now that we know the behaviour of simple RF fields in the rotating reference, let's take a look at the spin movements under an applied RF field. Suppose that we have a static field $\mathbf{B_0}$, a circularly polarized field $\mathbf{B_1}$ described as above with frequency $\boldsymbol{\omega}$, and let's use the rotating reference also with frequency $\boldsymbol{\omega}$. The equation of motion for the spins is then the following:

$$\left.\frac{\mathrm{d}\boldsymbol{\mu}}{\mathrm{d}t}\right|_{\text{rotating}} = \gamma \boldsymbol{\mu} \times \mathbf{B_{eff}} = \gamma \boldsymbol{\mu} \times \left(\mathbf{B_0} + \frac{\boldsymbol{\omega}}{\gamma} + \mathbf{B_1}\right) \tag{2.25}$$

To determine the allover angular frequency of the spins, take a look at the components of the effective magnetic field:

$$\mathbf{B_{eff}} = \mathbf{e'_z}\left(B_0 + \frac{\omega}{\gamma}\right) + \mathbf{e'_x} b_1 \tag{2.26}$$

From this we can easily get the effective angular momentum of the spins in the rotating reference, as it equals to $-\gamma \mathbf{B_{eff}}$. For the consequent notation, we define another angular frequency-like quantity: $\omega_1 \equiv -\gamma b_1$. Note: this it NOT the same as the RF frequency $\omega$. From here, the derivation of the effective angular frequency of the spins is straightforward:

$$\boldsymbol{\omega_{eff}} = \mathbf{e'_z}\Big(-\gamma B_0 - \omega\Big) - \mathbf{e'_x}\gamma b_1 = \mathbf{e'_z}\big(\omega_0 - \omega\big) + \mathbf{e'_x}\omega_1 \tag{2.27}$$

Just to be clear, we hereby repeat the meaning of all $\omega$-s in (2.27): $\omega_0$ is the precessing frequency around $\mathbf{B_0}$ (also called Larmor frequency), $\omega$ is the frequency of the RF field and also of the rotating reference, and finally, $\omega_1$ equals to $-\gamma b_1$.

The case when the Larmor frequency equals to the RF frequency, that is, $\omega_0 = \omega$ is called resonance. If this occurs, the situation becomes quite simple:

$$\mathbf{B_{eff}} = \mathbf{e}'_{\mathbf{x}} b_1 \tag{2.28}$$

$$\left.\frac{\mathrm{d}\boldsymbol{\mu}}{\mathrm{d}t}\right|_{\text{rotating}} = \gamma\boldsymbol{\mu} \times \mathbf{B_{eff}} = \boldsymbol{\mu} \times \mathbf{e}'_{\mathbf{x}} \gamma b_1 = -\omega_1 \boldsymbol{\mu} \times \mathbf{e}'_{\mathbf{x}} \tag{2.29}$$

Equation (2.29) desrcibes a precession solely around the $x'$ axis of the rotating frame. In other words, we can rotate the spins around the $x'$ axis of the rotating system by applying an oscillating magnetic field on the Larmor frequency. The angle alteration after such a pulse lasts for time $\tau$ is $\Delta\theta$ as can be seen in (2.30) and in Figure (2.3):

$$\Delta\theta = \gamma b_1 \tau \tag{2.30}$$

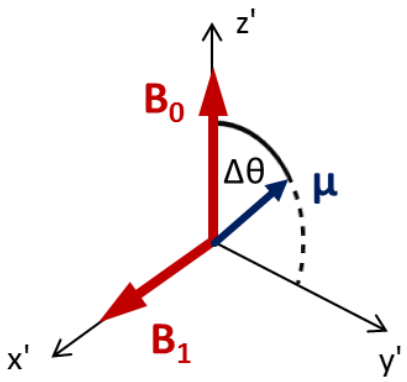


Figure 2.3: Rotation of the magnetic moment around the $x'$ axis in the rotating frame caused by resonant RF field

## 2.3 Relaxation processes

In the first part of this section I will present a fairly intuitive deduction of the spin-latice relaxation time $T_1$ without the claim of exactness followed by the empirical introduction of spin-spin relaxation time $T_2$. It is not an aim in this section, nor in this whole thesis, to provide a deep analysis of the relaxation physics, instead it intends to give a brief insight to the basic idea of these processes with a simple model. For more comprehensive information on this topic I suggest the literature, eg. [6] or [9].

At first, we introduce a quantity that plays important role in magnetic resonance called magnetization. Magnetization is defined by the net magnetic moment per unit volume, that is:

$$\mathbf{M} = \frac{1}{V}\sum_i \boldsymbol{\mu_i} \tag{2.31}$$

Where $i$ runs on all the magnetic moments in the volume. In this interpretation the volume V has to be small enough for the magnetization to be a function of space, and big enough to contain a large number of moments. In the following chapters we will usually use magnetization vector to describe the the time evolution of the system, but first we examine the basic concepts of relaxation.

## $T_1$ relaxation

It is known by many experimental results that if a bunch of magnetic moments are placed in external magnetic field, a certain part of these moments will align to the direction of the field. If we are talking about quantum mechanical objects, for example spin-half particles, this means that in the equilibrium state of the system a bit more than half of the spins will be parallel to the external field, and a bit less than half of them will be antiparallel to it. The ratio of these two depends on their energy level in the magnetic field, which is of course determined by the projection of the angular momentum to the field:

$$E_m = -\gamma\hbar B_0 m = \pm\frac{1}{2}\gamma\hbar B_0 \tag{2.32}$$

And the equilibrium ratio of the parallel ($N_+$) and antiparallel ($N_-$) spins is the well-known Boltzmann factor with the energy level difference:

$$\frac{N_-}{N_+} = \mathrm{e}^{-\frac{\Delta E}{k_B T}} = \mathrm{e}^{-\frac{\gamma\hbar B_0}{k_B T}} \tag{2.33}$$

If we alternate the ratio for example by applying an RF excitation the system will somehow return to the equilibrium state described in (2.33) after the excitation effect ceases. In a simple model where we assume the spins to be completely independent we can describe the relaxation method by two transition probabilities per unit time: the probability of a parallel spin becoming antiparallel $\left(N_+ \to N_-\right)$ denoted by $W\downarrow$, and the probability of the opposite, i. e. an antiparallel spin becoming parallel $\left(N_- \to N_+\right)$ denoted by $W\uparrow$. Note that these two are generally not equal because of the environment of the spins end the existence of the external magnetic field. With these probabilities, the time derivatives of the spin population can be written as:

$$\frac{\mathrm{d}N_+}{\mathrm{d}t} = -N_+ W\downarrow + N_- W\uparrow \tag{2.34a}$$

$$\frac{\mathrm{d}N_-}{\mathrm{d}t} = N_+ W\downarrow - N_- W\uparrow \tag{2.34b}$$

The measureable quantity is the difference between these populations, so we will use the followings:

$$n = N_+ - N_- \tag{2.35a}$$

$$N = N_+ + N_- \tag{2.35b}$$

Using (2.34) the time derivative of the population difference will be:

$$\frac{\mathrm{d}n}{\mathrm{d}t} = N\big(W\uparrow - W\downarrow\big) - n\big(W\uparrow + W\downarrow\big) \tag{2.36}$$

Whereof the equilibrium value of the population difference is

$$n_0 = \frac{N\big(W\uparrow - W\downarrow\big)}{\big(W\uparrow + W\downarrow\big)} \tag{2.37}$$

From this we define a time-dimension quantity as

$$T_1 \equiv \frac{1}{\big(W\uparrow + W\downarrow\big)} \tag{2.38}$$

Using this $T_1$ the time derivative of the population difference is as follows:

$$\frac{\mathrm{d}n}{\mathrm{d}t} = \frac{n_0 - n}{T_1} \tag{2.39}$$

With the solution of

$$n(t) = n(0)\mathrm{e}^{-\frac{t}{T_1}} + n_0\left(1 - \mathrm{e}^{-\frac{t}{T_1}}\right) \tag{2.40}$$

As can be seen, the time dependence of the spin population difference - with the latter proportional to the longitudinal component of the magnetization pointing to the direction of the external field - shows exponential decay to the equilibrium state with a time constant $T_1$. This effect is called longitudinal or $T_1$ relaxation.

### $T_2$ relaxation

The other relaxation process called transverse or $T_2$ relaxation will be presented here intuitively in a classical model. Assume we have a bunch of magnetic moments originally point to the direction of the external field, then we rotate them to the transverse plane with an RF pulse. The local magnetic field a specific spin experiences is the sum of the external field and the small fields of the neighbouring spins. The latter small fields vary in space that leads to different local precession frequencies. Therefore the spins tend to fan out in time as shown in Figure 2.4, this is usually called dephasing. Since the measureable

magnetization is the vector (or complex - see (2.14)) sum of the individual magnetic moments, the net magnetization decreases over time. This reduction brings forth another exponential decay with characteristic time $T_2$ that adds to the time derivative of the transverse component of the magnetization. We can express it by adding an exponential term to (2.13) written with magnetization instead of a single moment. In the laboraroty frame:

$$\left.\frac{\mathrm{d}\mathbf{M}_\perp}{\mathrm{d}t}\right|_{\mathrm{lab}} = \gamma\mathbf{M}_\perp \times \mathbf{B} - \frac{\mathbf{M}_\perp}{T_2} \tag{2.41}$$

And in the rotating system:

$$\left.\frac{\mathrm{d}\mathbf{M}_\perp}{\mathrm{d}t}\right|_{\mathrm{rot}} = \gamma\mathbf{M}_\perp \times \mathbf{B}_{\mathbf{eff}} - \frac{\mathbf{M}_\perp}{T_2} \tag{2.42}$$

If the frequency of the rotating frame equals to the Larmor frequency and there are no other magnetic fields like RF excitation then the effective field becomes zero and the solution of (2.42) become a simple exponential decay:

$$M_\perp(t) = M_\perp(0)\mathrm{e}^{-\frac{t}{T_2}} \tag{2.43}$$

## $T_2^*$ decay

In practice however, there is an additional dephasing of moments caused by the inhomogeneities of the external field itself that also reduces net magnetization. Therefore the total reduction of the transverse component of magnetization over time is the resultant of the above described $T_2$ relaxation and this new process caused by the external field inhomogeneities. The latter is called $T_2'$ relaxation and usually also acts as an exponential reduction with a time constant $T_2'$. The sum of these two effects results in another exponential decay with characteristic time $T_2^*$ given by the following:

$$\frac{1}{T_2^*} = \frac{1}{T_2} + \frac{1}{T_2'} \tag{2.44}$$

In the formula above the reciprocals of characteristic times are usually referred to as relaxation rates, so (2.44) says that the relaxation rates simply add up.

Now that we introduced the relaxation effects, we can construct the total system of equations of motion for a static field. Assume we have a static and perfectly homogeneous magnetic field (so there is no $T_2'$ dephasing) points to the $z$ direction. Then the equations in the laboratory frame:

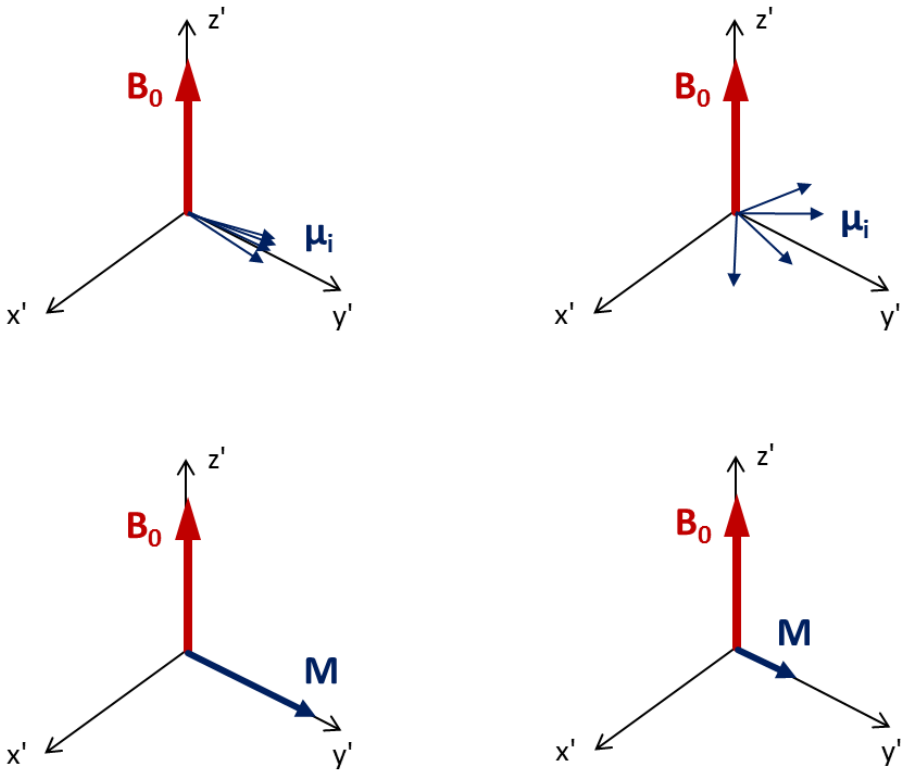


Figure 2.4: Dephasing of the individual moments in the rotating frame and the decreasing net magnetization as a result.

$$\frac{\mathrm{d}M_x}{\mathrm{d}t} = \omega_0 M_y - \frac{M_x}{T_2} \tag{2.45a}$$

$$\frac{\mathrm{d}M_y}{\mathrm{d}t} = -\omega_0 M_x - \frac{M_x}{T_2} \tag{2.45b}$$

$$\frac{\mathrm{d}M_z}{\mathrm{d}t} = \frac{M_0 - M_z}{T_1} \tag{2.45c}$$

By using the complex formalism introduced at (2.14) the first two coupled equation will become one complex equation:

$$M_+ = M_x + \mathrm{i}M_y \tag{2.46}$$

$$\frac{\mathrm{d}M_+}{\mathrm{d}t} = -\mathrm{i}\omega_0 M_+ - \frac{M_+}{T_2} \tag{2.47}$$

And the solution with this complex description will be

$$M_+(t) = M_+(0)\mathrm{e}^{-\mathrm{i}\omega_0 t - \frac{t}{T_2}} \tag{2.48a}$$

$$M_z(t) = M_z(0)\mathrm{e}^{-\frac{t}{T_1}} + M_0\left(1 - \mathrm{e}^{-\frac{t}{T_1}}\right) \tag{2.48b}$$

## 2.4 Signal detection

In the previous sections we have focused on the effects of external fields to magnetic moments and the time evolution of the magnetization. Now we proceed to the question how can this precessing magnetization be measured. The answer is, of course, induction. The fundamental idea is to rotate the spins from their equilibrium direction to the transverse plane with an applied RF pulse and measure the voltage induced by the precessing magnetization in the coil around the sample. In the followings the detailed deduction of the induced signal is presented.

From the integral form of the 3rd Maxwell equation [7] we know that a time-varying magnetic flux induces electromotive force (emf or simply voltage) in a coil:

$$U = -\frac{\mathrm{d}\Phi}{\mathrm{d}t} \tag{2.49}$$

The magnetic flux can be computed with the integration of magnetic field on a surface, but sometimes it is more convenient to use the Stokes theorem to calculate the flux by the integration of the vector potential on a closed line bounding the desired surface.

$$\mathbf{B} = \nabla \times \mathbf{A} \tag{2.50}$$

$$\Phi = \int \mathbf{B}\mathrm{d}\mathbf{S} = \oint \mathbf{A}\mathrm{d}\mathbf{l} \tag{2.51}$$

When dealing with conventional electric currents, the vector potential can be calculated with the current density:

$$\mathbf{A}(\mathbf{r}, t) = \frac{\mu_0}{4\pi} \int \frac{\mathbf{J}(\mathbf{r}', t)}{|\mathbf{r} - \mathbf{r}'|} \mathrm{d}^3\mathrm{r}' \tag{2.52}$$

But we do not have real electric currents, only magnetization. However, from the differential form of the 4th Maxwell equation and the definition of the magnetizing field [7] we can construct a current density associated with magnetization.

$$\mathbf{H} = \frac{\mathbf{B}}{\mu_0} - \mathbf{M} \tag{2.53}$$

$$\nabla \times \mathbf{H} = \mathbf{J} + \frac{\partial \mathbf{D}}{\partial t} \tag{2.54}$$

$$\mathbf{J}_\mathbf{M} = \nabla \times \mathbf{M} \tag{2.55}$$

Substituting this to (2.52) and (2.51) we get an expression to magnetic flux containing the magnetization:

$$\Phi = \oint \mathrm{d}\mathbf{l}\left(\frac{\mu_0}{4\pi}\int \mathrm{d}^3\mathrm{r}'\frac{\mathbf{J_M}(\mathbf{r}',t)}{|\mathbf{r}-\mathbf{r}'|}\right) = \oint \mathrm{d}\mathbf{l}\left(\frac{\mu_0}{4\pi}\int \mathrm{d}^3\mathrm{r}'\frac{\nabla\times\mathbf{M}(\mathbf{r}',t)}{|\mathbf{r}-\mathbf{r}'|}\right) \tag{2.56}$$

Using integration by parts and leaving the surface terms as there are no magnetization in the infinitely far point:

$$\Phi = \frac{\mu_0}{4\pi}\int \mathrm{d}^3\mathrm{r}' \oint \mathrm{d}\mathbf{l}\left[\left(-\nabla'\frac{1}{|\mathbf{r}-\mathbf{r}'|}\right)\times\mathbf{M}(\mathbf{r}',t)\right] \tag{2.57}$$

We can now use the vector identity $\mathbf{a}(\mathbf{b}\times\mathbf{c}) = \mathbf{b}(\mathbf{c}\times\mathbf{a})$ and get:

$$\Phi = \int \mathrm{d}^3\mathrm{r}'\mathbf{M}(\mathbf{r}',t)\underbrace{\left[\nabla\times\oint\frac{\mu_0}{4\pi}\frac{\mathrm{d}\mathbf{l}}{|\mathbf{r}-\mathbf{r}'|}\right]}_{\mathcal{B}^{rec}} \tag{2.58}$$

If we compare the term marked as $\mathcal{B}^{rec}$ in (2.58) with (2.50) and (2.52) it becomes clear that this $\mathcal{B}^{rec}$ tells us the effectiveness of the coil at the point $\mathbf{r}$, i. e. the magnetic field generated at the point $\mathbf{r}$ with a unit current flowing in the coil. Because of the invariance of Maxwell's equations to a time reversal transformation, this coil efficiency also characterizes the receiving sensitivity, i. e. if there is a time-varying magnetic moment at point $\mathbf{r}$, it induces an electromotive force in the coil proportional to $\mathcal{B}^{rec}$. This statement, also referred to as the *principle of reciprocity*, I will not justify in this thesis; a detailed explanation can be found in [6] or [10].

Now we have our expression for the magnetic flux with the receiving sensitivity $\mathcal{B}^{rec}$. The signal we measure both in NMR and MRI is the voltage induced by the precessing magnetization in the coil(s) around the sample or the patient. Therefore our signal $S$ will be proportional to the time derivative of the magnetic flux in (2.58) (the proportionality factor usually differs from 1 because of the measurement electronics):

$$S \propto -\frac{\mathrm{d}}{\mathrm{d}t}\int \mathrm{d}^3\mathrm{r}\mathbf{M}(\mathbf{r},t)\mathcal{B}^{rec}(\mathbf{r}) \tag{2.59}$$

The magnetization contains two types of time dependence: the Larmor precession and the exponential decays. The frequencies associated with these terms are in the order of magnitude of 10-100 Hz and 100MHz, respectively. Therefore the time derivative of the exponential decays are negligible beside the Larmor precession, so one can say that only the precession gives contribution to the signal. It implies that we can only measure the transversal components of the magnetization, or in the complex formalism, $M_+$. As a reminder the time and space dependence of this is:

$$M_+(\mathbf{r},t) = M_+(\mathbf{r},0)\mathrm{e}^{-\mathrm{i}\omega_0 t - \frac{t}{T_2(\mathbf{r})}} \tag{2.60}$$

So our signal will be:

$$S \propto \omega_0 \int \mathrm{d}^3\mathrm{r}\, \mathrm{e}^{-\frac{t}{T_2(\mathbf{r})}} \left[ \mathcal{B}_x^{rec}(\mathbf{r}) \Re\Big( \mathrm{i} M_+(\mathrm{r},t)\mathrm{e}^{-\mathrm{i}\omega_0 t} \Big) + \mathcal{B}_y^{rec}(\mathbf{r}) \Im\Big( \mathrm{i} M_+(\mathrm{r},t)\mathrm{e}^{-\mathrm{i}\omega_0 t} \Big) \right] \tag{2.61}$$

For the complex description to work we also define the transversal component of $\mathcal{B}^{rec}$ denoted by $\mathcal{B}_\perp^{rec}$, and write up the $x$ and $y$ components with this:

$$\mathcal{B}_x^{rec} = \mathcal{B}_\perp^{rec} \cos(\theta_B) \tag{2.62a}$$

$$\mathcal{B}_y^{rec} = \mathcal{B}_\perp^{rec} \sin(\theta_B) \tag{2.62b}$$

Using this method the signal will be the following:

$$S \propto \omega_0 \int \mathrm{d}^3\mathrm{r}\, \mathrm{e}^{-\frac{t}{T_2(\mathbf{r})}} M_\perp(\mathbf{r},0) \mathcal{B}_\perp^{rec}(\mathbf{r}) \sin\Big( \omega_0 t + \theta_B(\mathbf{r}) - \phi_0(\mathbf{r}) \Big) \tag{2.63}$$

In the spatially independent limit, i. e. when everything in (2.63) is independent from $\mathbf{r}$ the signal will be as follows:

$$S \propto \omega_0 V_{\text{sample}} \mathrm{e}^{-\frac{t}{T_2}} M_\perp \mathcal{B}_\perp^{rec} \sin\Big( \omega_0 t + \theta_B - \phi_0 \Big) \tag{2.64}$$

## Signal demodulation

In practice the signal deduced in the previous section is not visualised as it is, but instead the NMR or MRI instrument eliminates the frequency offset $\omega_0$ by demodulating the signal. It is done by multiplying the signal in (2.63) with harmonics of frequency $\Omega$ that is close to the Larmor frequency $\omega_0$. That is, $\Omega = \omega_0 + \delta\omega$. In this way a complex signal is created: the real part will be when the sign is multiplied with $\sin(\Omega t)$, and the imaginary part arises as the multiplication of the signal and $\cos(\Omega t)$.

The real part of the demodulated signal (often called as the "real channel") will be:

$$\sin\big(\omega_0 t + \theta_B - \phi_0\big) \sin\Big( (\omega_0 + \delta\omega) t \Big) = \frac{1}{2} \Big[ \cos\big( \delta\omega t - \theta_B + \phi_0 \big) - \cos\Big( (2\omega_0 + \delta\omega) t + \theta_b - \phi_0 \Big) \Big] \tag{2.65}$$

After the multiplication the part with frequency $2\omega_0 + \delta\omega$ is removed with a lowpass filter, and the remaining low-frequency term forms the real channel of the signal.

$$S_{\text{Re}} \propto \frac{1}{2} \cos\big( \delta\omega t - \theta_b + \phi_0 \big) = \frac{1}{2} \Re\Big( \mathrm{e}^{-\mathrm{i}\delta\omega t - \mathrm{i}\theta_B + \mathrm{i}\phi_0} \Big) \tag{2.66}$$

The imaginary channel is quite similar. After the multiplication with $\cos\big(\Omega t\big)$ and the lowpass filtering:

$$S_{\mathrm{Im}} \propto \frac{1}{2}\sin\big(\delta\omega t - \theta_b + \phi_0\big) = \frac{1}{2}\Im\Big(\mathrm{e}^{-\mathrm{i}\delta\omega t - \mathrm{i}\theta_B + \mathrm{i}\phi_0}\Big) \tag{2.67}$$

So the detected signal managed as complex is:

$$S \propto \omega_0 \int \mathrm{d}^3\mathrm{r}\, \mathrm{e}^{-\frac{t}{T_2(\mathbf{r})}} M_\perp(\mathbf{r}) \mathcal{B}_\perp^{rec}(\mathbf{r},0) \mathrm{e}^{-\mathrm{i}\left(\delta\omega t + \theta_B(\mathbf{r}) - \phi_0(\mathbf{r})\right)} \tag{2.68}$$

## 2.5 Fundamental pulse sequences: Free Induction Decay and Spin Echo

As we have seen in the previous chapters we can rotate the spins - and the magnetization - from their equilibrium state with an arbitrary angle by applying an appropriate Larmor-frequency RF field for length of time determined by (2.30). We have also learned that if the magnetization has transverse component then it will precess with Larmor frequency and induce measureable electromotive force in a nearby coil. Therefore with a suitable sequence of RF fields and coil voltage measurements we can investigate the magnetization of the sample. In MR technology the RF fields that rotate the magnetization are called *pulses* while the detection, demodulation and digitalization of the induced voltage signal is referred to as *acquisition*. The whole process containing the RF pulses and acquisitions is called *pulse sequence*. In this section two basic pulse sequency is presented, free induction decay, usually referred to as FID, and spin echo, sometimes abbreviated as SE. The sequences will be graphically presented by the so-called sequence diagrams, which represent the RF pulses and acquisitions in a schematic form.

### Free Induction Decay

In the FID pulse sequence the situation is quite simple. We apply an RF pulse to rotate the magnetization with 90 degrees so the transverse component will be maximal and the longitudinal component becomes zero. Then as the spins precess, the acquisition is turned on to measure the induced signal until it vanishes due to $T_2^*$ decay. The sequence diagram of the FID is shown in Figure 2.5.

As was mentioned in section 2.3, the $T_2^*$ decay in the FID experiment comes from two components, the $T_2$ of spin-spin relaxation and the $T_2'$ due to external field inhomogeneities. To get a clue of the practical values of this $T_2^*$ we here present an estimation of the dephasing time $T_2'$.

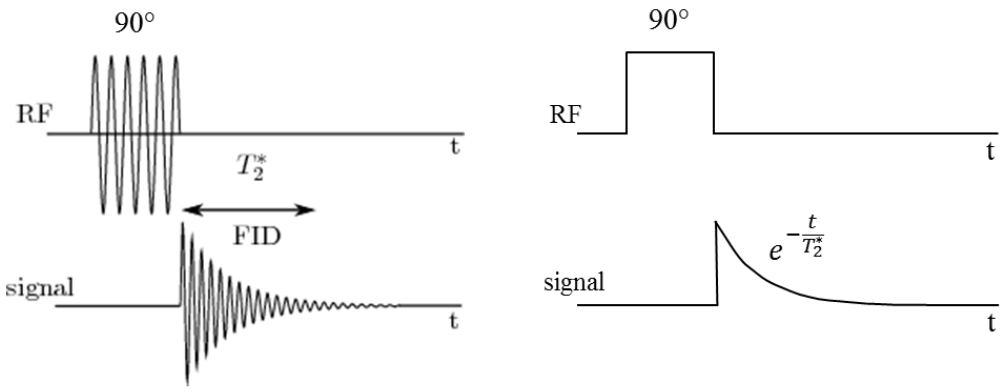


Figure 2.5: Sequence diagram of a free induction decay experiment. Left: RF pulse and signal in the laboraroty frame of reference. Right: RF pulse and signal in the rotating frame, i.e. the demodulated signal with the offset frequency $\delta\omega = 0$. Note that the laboratory signal on the left is only suggestive since the real Larmor oscillation frequency is far too large to display.

Assume we have an external field of 1.5 T with a homogeneity of 1 point per million (ppm), and we are performing NMR experiment on protons. One can say that the FID signal disappears roughly when the spins have gained a phase difference of $\pi$. We can calculate the time $\tau$ needed for this from the following:

$$\gamma(\Delta B_0)\tau = \pi \tag{2.69}$$

$$42.58[\text{MHz/T}] \times 2\pi \times 1.5[\text{T}] \times 1[\text{ppm}] \times \tau = \pi \tag{2.70}$$

$$\tau \approx 7.8\,\text{ms} \tag{2.71}$$

As can be seen, an inhomogeneity as small as 1 ppm eliminates the signal in less than 10 ms in a device with the commonly used 1.5 T.

## Spin Echo

Although we have seen that the signal vanishes really fast even with a very little inhomogeneity in the main field, the situation is not as bad as one may think based on this. It is because Hahn et al. [5] found that the eliminated signal is retrievable by an RF pulse trick.

As mentioned before, the signal elimination is caused by two effects. First, the individual spins experience the small magnetic fields of their neighbours, which adds to the

external field causing the local Larmor frequencies to vary spatially and the precessing spins to dephase. These spin-spin interactions also evolve in time really fast, making this $T_2$ dephasing irreversible. However, the situation differs at the dephasing caused by the external field inhomogeneities. These field variations remain constant in time and thus the dephasing caused by them could be reversed by the negation of the phase of each spin.

The idea is the following. With an RF pulse we rotate the spins with 90° to the transverse field. At this point every spin points at the same direction, or in the complex description, they all have the same phase when they start to precess in the slightly inhomogeneous main field. After that if a spin experiences a larger external field and precesses at a higher frequency for the length of time $\tau$, it accumulates a positive relative phase $\phi$ according to spins preseccing at the center frequency. Then we apply another RF pulse of 180° which will turn the spins around and negates their phase. For example the previously described spin that gained $\phi$ phase in time interval $\tau$ will have the relative phase $-\phi$ right after the 180° pulse. Of course this spin will continue to experience a larger field regardless of the applied 180° pulse, and therefore its relative phase continues to grow in time. After another time interval $\tau$ it will have zero relative phase again. Since we did not use any specific parameter of the picked spin nor of the field, this thread is applicable to all spins in the sample. So at the time $\tau$ after the 180° pulse all spins will have the same phase (will point to the same direction) creating a macroscopic magnetization once again, which can be measured.

What we get as a result was quite astonishing at the time of its invention: the MR signal eliminated by $T_2^*$ dephasing is retrievable by a 180° RF pulse. The latter is called refocusing pulse, the recurring signal after the 180° pulse is called a spin echo, and the total time between the 90° pulse and the echo is referred to as echo time $T_E$. The scheme of the process is shown in Figure 2.6 [11].

Note that the above are only valid for the dephasing caused by field inhomogeneities, and are not able to reverse the $T_2$ relaxation caused by spin-spin interactions. Therefore the recurring signal will be smaller then it was right after the 90° pulse as the signal amplitude is enveloped by the exponential decay $T_2$.

Knowing the above it is easy to interpret the sequence diagram of the spin echo experiment shown in Fig. 2.7.

Without the detailed deduction - that can be found in [6] - the expressions for the perfectly demodulated signal in spin echo sequence are the followings:

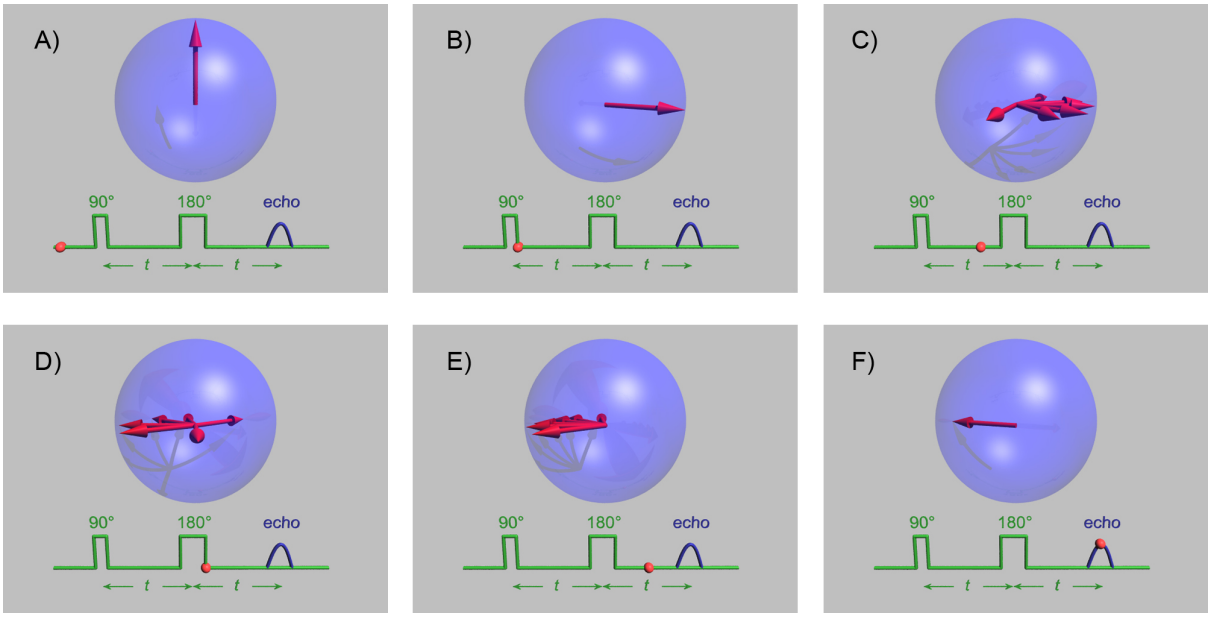


Figure 2.6: Scheme of the spin echo. A) The spins before the excitation. B) The spins after the 90° RF pulse. C) Dephased spins due to field inhomogeneities. D) The spins turned around by the 180° pulse that negates their phase. E) spins are rephasing after the refocusing pulse. F) Refocused spins and the spin echo. Figure copyright and license details at [11].

$$M_{\perp}(t) = M_{\perp}(0) \times \begin{cases} \mathrm{e}^{-\frac{t}{T_2^*}} & 0 < t < \tau \\ \mathrm{e}^{-\frac{t}{T_2}}\,\mathrm{e}^{-\frac{T_E - t}{T_2'}} & \tau < t < 2\tau = T_E \\ \mathrm{e}^{-\frac{t}{T_2}}\,\mathrm{e}^{-\frac{t - T_E}{T_2'}} & T_E < t \end{cases} \tag{2.72}$$

The spin echo sequence has the significant advantage that the appearance of the signal (the echo) and the RF pulses are separated in time, unlike in FID where the signal appears right after the RF excitation. This is a great benefit since (with a one-channel device) we cannot measure the induced signal during the RF pulse, nor in a certain time interval after it - we would only see the voltage induced in the receiving coil by the RF field itself.

## 2.6 Basic principles of magnetic resonance imaging

In this chapter the basic principles of MR imaging is presented. We will start at the demodulated complex signal of the precessing spins as it was at the end of section 2.4:

$$S \propto \omega_0 \int \mathrm{d}^3\mathrm{r}\, \mathrm{e}^{-\frac{t}{T_2(\mathbf{r})}} M_{\perp}(\mathbf{r}, 0) \mathcal{B}_{\perp}^{rec}(\mathbf{r}) \mathrm{e}^{-\mathrm{i}\left(\delta\omega t + \theta_B(\mathbf{r}) - \phi(\mathbf{r}, t)\right)} \tag{2.73}$$

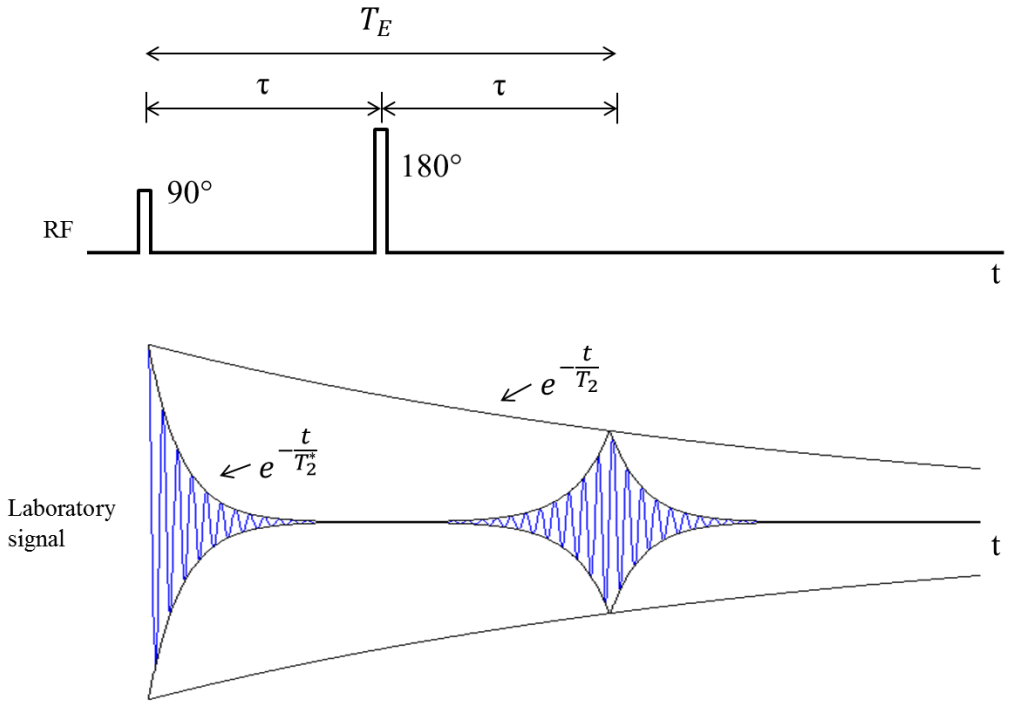


Figure 2.7: Sequence diagram of a spin echo experiment. Note how the signal is enveloped by the $T_2$ relaxation.

For the simplicity of the description, from now on we will assume the followings:

- Appropriate RF coil, i. e. spatially independent $\mathcal{B}^{rec}$ and $\theta_B$
- The proportionality factors in (2.73) are summed up in one factor $\Lambda$
- Relaxation effects are negligible since the relevant imaging process is fast related to their characteristic times
- the signal demodulation is perfect, i. e. $\delta\omega = 0$

Provided these the signal takes the following form:

$$S = \Lambda\omega_0\mathcal{B}_\perp^{rec}\int \mathrm{d}^3\mathrm{r}\; M_\perp(\mathbf{r},0)\mathrm{e}^{\mathrm{i}\phi(\mathbf{r},t)} \tag{2.74}$$

Without a detailed explanation - that can be found in [6] - the equilibrium value of the magnetization can be estimated as:

$$M_0 = \rho_0\frac{S(S+1)\gamma^2\hbar^2}{3k_BT}B_0 \tag{2.75}$$

The factor in (2.75) is the well-known Curie susceptibility with $S = \frac{1}{2}$ for proton and $\rho_0$ is the spatial spin density. As $M_\perp$ in equation (2.74) means the amplitude of the

transverse component right after the 90° pulse, it can be well approximated with the equilibrium magnetization $M_0$ expressed in (2.75). Therefore, our signal can be written as the following.

$$S = \Lambda\omega_0 \mathcal{B}_\perp^{rec} \frac{1}{4} \frac{\gamma^2\hbar^2}{k_B T} B_0 \int \mathrm{d}^3\mathrm{r}\, \rho_0(\mathbf{r}) \mathrm{e}^{\mathrm{i}\phi(\mathbf{r},t)} \tag{2.76}$$

This can be simplified by introducing the so-called effective spin density $\rho(\mathbf{r})$:

$$\rho(\mathbf{r}) = \Lambda\omega_0 \mathcal{B}_\perp^{rec} \frac{1}{4} \frac{\gamma^2\hbar^2}{k_B T} \rho_0(\mathbf{r}) B_0 \tag{2.77}$$

$$S = \int \mathrm{d}^3\mathrm{r}\, \rho(\mathbf{r}) \mathrm{e}^{\mathrm{i}\phi(\mathbf{r},t)} \tag{2.78}$$

As can be seen, the measureable signal is finally made up of the phase-correct sum of the effective spin density.

This is the point where move to the concept that fundamentally distinguishes imaging tecniques from traditional NMR experiments - the idea of gradient fields, and their effect to the magnetization phase.

If the main field $B_0$ is perfectly homogeneous and the signal demodulation is complete then the phase term in (2.78) becomes time-independent as all the spins will precess with the same Larmor frequency. Moreover, if we define the starting time to be at the end of the 90° pulse, or as also referred, the excitation, then all the spins will point to the same direction, meaning all of them will have the same phase at $t = 0$. In this case the phase term will also be spatially independent.

$$\phi(\mathbf{r}, t) = \phi(\mathbf{r}, 0) = \phi_0 \tag{2.79}$$

However if our main field is not the same everywhere then the phase of a certain spin will change in time with the local difference of the larmor frequency:

$$\phi(\mathbf{r}, t) = \int_0^t \Delta\omega(\mathrm{r}, t')\mathrm{d}t' = -\gamma \int_0^t \big[B(\mathbf{r}, t') - B_0\big]\mathrm{d}t' \tag{2.80}$$

The idea is the following. Let's add an additional field to the main field $B_0$ which is not homogeneous but varies linearly in space. This new field is referred to as the gradient field and is characterised by its spatial gradient $\mathbf{G}$.

$$\mathbf{B} = \big(0, 0, B(\mathbf{r}, t)\big) \tag{2.81}$$

$$\mathbf{G}(t) = \nabla B(\mathbf{r}, t) \tag{2.82}$$

$$B(\mathbf{r},t) = B_0 + \mathbf{G}(t)\mathbf{r} \tag{2.83}$$

With this gradient field existing the spin phases will develop in a manner defined by the gradient field.

$$\phi(\mathbf{r},t) = \int_0^t \Delta\omega(\mathrm{r},t')\mathrm{d}t' = -\gamma \int_0^t \big[B(\mathbf{r},t') - B_0\big]\mathrm{d}t' = -\gamma\mathbf{r}\int_0^t \mathbf{G}(t')\mathrm{d}t' \tag{2.84}$$

Here we define a new vector $\mathbf{k}$ which will eventually play an extremely important role in the imaging process.

$$\mathbf{k} \equiv \frac{\gamma}{2\pi}\int_0^t \mathbf{G}(t')\mathrm{d}t' = \gamma \int_0^t \mathbf{G}(t')\mathrm{d}t' \tag{2.85}$$

As shown, this $\mathbf{k}$ is defined by the time integral of the gradient and therefore can be easily manipulated by switching different gradients on and off. In the second equation in (2.85) we have introduced a new notation: $\gamma$ equals to $\frac{\gamma}{2\pi}$ and is called the reduced gyromagnetic ratio.

With this new vector $\mathbf{k}$ the spin phases can be expressed quite simple:

$$\phi(\mathbf{r},t) = -2\pi\mathbf{k}\mathbf{r} \tag{2.86}$$

By substituting this into (2.78) we get an astonishing outcome:

$$S = \int \mathrm{d}^3\mathrm{r}\ \rho(\mathbf{r})\mathrm{e}^{-\mathrm{i}2\pi\mathbf{k}\mathbf{r}} = \mathcal{F}\left\{\rho(\mathbf{r})\right\} \tag{2.87}$$

The result in (2.87) is of enormous importance. It tells us that by the use of appropriate gradient fields the connection between the acquired signal and the spatial effective spin density, or in other words, the image of the sample or the patient, becomes the well-known and easy-to-compute operation, the Fourier transformation. In this interpretation the previously defined vector $\mathbf{k}$ gains a new meaning: this is the spatial frequency, the conjugate of the spatial coordinate $\mathbf{r}$.

Therefore to get an image we just have to apply the gradient fields in a way to achieve a sufficient set of $\mathbf{k}$ vectors and then perform an inverse Fourier transform on the acquisited signal. In this way our signal is no longer a function of time, but a function of the spatial frequency $\mathbf{k}$.

$$\rho(\mathbf{r}) = \mathcal{F}^{-1}\left\{S(\mathbf{k})\right\} \tag{2.88}$$

To put this concept into a form easier to imagine, the alignment of the spins before and after the application of a gradient for a certain time is illustrated in Figure 2.8. On the left, before the gradient effect, all the spins point to the same direction, i. e. they all have the same phase. On the right we can see the spins after some time in the upwards-pointing gradient field and therefore folded into a helix. This is because the magnetic field and thus the Larmor frequency vary linearly along the direction of the gradient, causing the spins to accumulate a phase depeding linearly on their position. If the gradient field continiues to exist the helix will have more and more twists on the same length as time elapses, accordingly to the growth of the spatial frequency.

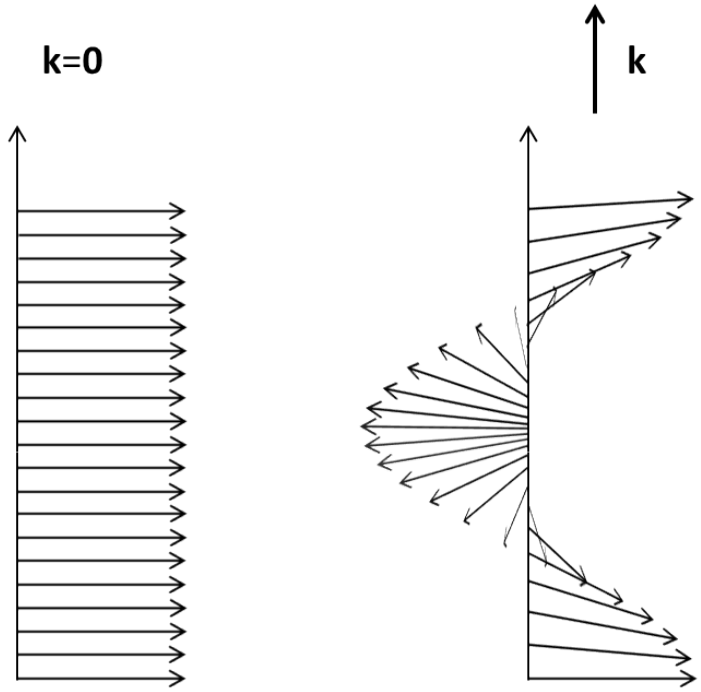


Figure 2.8: Effect of the gradient field. Left: Aligned spins before the gradient. Right: Spins folded into a helix after the application of a gradient field pointing upwards.

# 3. About the used NMR spectrometer

During our work we used a Bruker UltraShield 300 NMR magnet of 7T with a Bruker Avance DRX 400 spectrometer. The main field is generated by current flowing in a type 2 superconducting coil diving in liquid Helium for cooling. There is also an outer liquid Nitrogen tank to lower the thermal gradient between the Helium and the outer air. The device is shown in Figure 3.1.


Figure 3.1: The used NMR spectrometer (right) and the shielded superconducting magnet (left).

The magnet has a field strength of 7T providing excellent signal-to-noise ratio and requires the use of high frequency circuits due to the large Larmor frequencies. Since this system was designed to chemical NMR measurements there are severe limitations for imaging purposes. The magnet has an inner bore diameter of 54 mm but this is reduced to 40 mm by the warm shim coil system. This consists of 26 independently controlled shim coils to correct the field inhomogeneities. Using these the inhomogeneity of the main field can be below 0.1 ppm in a fraction of a $cm^3$, however in imaging experiments when the sample volume is a few cubic centimetres the inhomogeneities are in the order of

magnitude of 1 ppm even with the use of shim coils. A more detailed description of the shim system can be found in the thesis of Gyula Gyebnár [12].

The spectrometer is capable to provide the excitation and to receive the signal in two independent channels. Both of the channels measure the demodulated signal as a complex value by quadrature detection described in section 2.4. The device is able to provide and receive the signal with an arbitrary phase shift, or in other words, in arbitrary direction in the rotating reference frame. This feature allows us to perform phase-cycling algorithms which we heavily used in our imaging sequences to avoid DC offsets.

The amplification of the excitation signal was done by either the amplifier designed for 300 MHz for proton (H) or the broadband amplifier designed for arbitrary nuclei (referred to as X). For the Sodium experiments we used the latter while the water samples had to be performed using the H amplifier as the other one was not able to operate in such high frequency as 300 MHz. The Sodium amplifier had a power of 100 W while the H one was of 50 W. However for stability reasons we used both amplifier with an attenuation of 6 dB, i. e. at fourth the power.

The spectrometer is controlled by a PC software called TopSpin. This program is higly targeted to spectroscopic measurements with an easy-to-use language and environment, but unfortunately this made it cumbersome to determine the exact role of the commands and it was extremely difficult to write an experiment method that does not fit into the spectroscopy logic.

# Part I

# The radiofrequency (RF) system

# 4. RF coils in magnetic resonance

The radiofrequency probe is the heart of all NMR experiments and MRI examinations. It is responsible for producing the transverse magnetic field for spin excitation, and the electromotive force arised by the precessing magnetization is also induced in it.

Both in NMR and MRI the RF circuit usually contians one or more coils to produce the $B_1$ field. However, the coil as a conductive structure opposes itself to the high frequency current due to its self-inductance. This coil reactance should be compensated with capative elements, which means that our probe becomes a resonator with a tuning frequency determined by its inductance and capacitance. To get a useful circuit one should adjust the resonance frequency to equal the larmor frequency of the desired nuclei in the given field strength.

Having a properly tuned resonator however is not sufficient in itself. This is because such a circuit usually has a large and complex impedance (Z), unlike the transmitter cable that usually has an impedance of $50\,\Omega$ ($Z_0$) without an imaginary part. The difference between these two impedance will cause the reflection of the signal according to the well-known formula:

$$R = \left| \frac{Z - Z_0}{Z + Z_0} \right| \tag{4.1}$$

To ensure the reflection coefficient R to be small we have used some additional elements that adjust the impedance of the resonator to $50\,\Omega$. This process, called matching, can be done either by capacitive or inductive way, however the former is more widespread in practice.

The simplest resonators used mainly in NMR techonogy consists a simple solenoid and two trimmer capacitors to adjust the tuning frequency and the impedance of the circuit. This scheme is shown in Figure 4.1.

In some cases the solenoid is replaced by some other coil design like the Hoult-Deslauriers [13] or some others, but a solenoid is often used in practice as well because of its fine $B_1$ homogeneity. The paper cited in [14] provides a broad description of RF coils.

However, the solenoid and many of the other designs have some serious disadvantages when it comes to imaging. At first, for imaging purposes we need coils with significantly larger volume in order to place the sample or patient in them, than we did for NMR experiments (in this thesis we focus on volume coils only). This is a problem because if we use bigger coils, their self-inductance will grow as well, and RF coils with large self-inductance are to be avoided. All in all, such solenoid-type RF coils are disadvantageous in MRI for at leats three reasons.

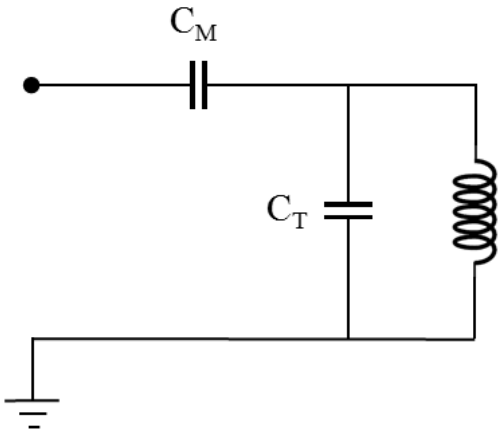


Figure 4.1: Simple RF circuit used in NMR experiments. The capacitor $C_T$ is mainly responsible for setting the tuning frequency while the one denoted by $C_M$ is used to match the impedance of the circuit.

First, to get a proper tuning frequency we have to use capacitors with smaller and smaller capacitance if the self-inductance of the coil becomes larger as the resonance frequency of a circuit is given by the formula $\omega = \frac{1}{\sqrt{LC}}$. After a point - in the order of magnitude of 1 pF - there is no capacitor commercially available and thus the desired tuning frequency is difficult to achieve.

Second, these coils produce magnetic field parallel to their axis. This geometry can lead to access problems in the magnet as most of the NMR devices and MRI scanners have a cylinder-like bore with an axis parallel to the main field. As we need transverse field from the RF coil, i. e. a field perpendicular to the main field, a solenoid would also have to be placed in the bore transversely, losing lots of free space and also the free in-vivo access to the inside of the RF coil.

Third, the coil will produce not just magnetic field, but also an electric field inside the sample or the patient. This is not the electric field generated by the time derivative of the magnetic field but the conservative electric field raised by the charges in the coil. This field will cause small currents in the patient heating the body, and also appear as a loss of power in the coil. Both of these effects are disadvantageous and become more significant as coil self-inductance grows.

Therefore it would be derisable to use coils that produce $B_1$ field perpendicular to their axis. In this way we could place the coil into the bore with the same axis and get free access to the inside of the coil. Fortunately, it is physically possible to construct coils of this kind. The idea is based on the fact that if a conducting cylinder has a sinusoidal current distribution on its surface with the current flowing parallel to the cylinder axis,

it will produce a homogeneous transverse magnetic field in the inside of the cylinder [17]. The concept is shown in Figure 4.2. Another benefit is that in this way coils with large volumes can be constructed with a relatively small self-inductance.

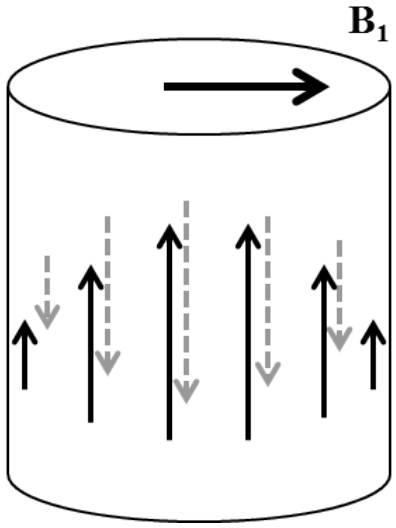


Figure 4.2: Conducting cylinder with a sinusoidal current distribution on its surface, producing a homogeneous transverse magnetic field in the inside.

There are numerous designs based on the idea of sinusoidal currents like the Saddle coil [15] or the Alderman-Grant resonator [16] but the one that became excessively widespread in imaging scanners is the Birdcage coil [17].

In the next section the mathematical model of the Birdcage coil is presented including the calculation of resonant modes with network analysis. The computation of inductance parameters from geometrical properties of the coil can be found in Appendix A.

## 4.1 The Birdcage coil

Since its invention in 1985 the Birdcage coil spread rapidly due to its highly homogeneus transverse magnetic field and preferable geometry. In the following years many approaches arose and have been applied to predict the resonant behavior of this coil from experimental methods to numerical simulations of its electromagnetic field. In the followings I present the structure of the Birdcage coil and provide a deduction of the resonant modes from the coil parameters by the eigenvalue method proposed by Mark C. Leifer [18].

The structure of the Birdcage coil is shown in Figure 4.3. As can be seen, the coil is made up of cunducting sections and capacitors forming a cylinder-like shape. The two ring-like ends of the coil are called endrings while the vertical parts are referred to as legs.

In general there are capacitors both in the endrings and in the legs, nonetheless there are variants of this design with endring or leg capacitors replaced with conducting wires, referred to as lowpass and highpass coils, respectively. As can be seen from Figure 4.3 the Birdcage coil with N legs has a discrete N-grip rotational symmetry as the capacitors are of the same value in the endrings and in the legs, separately. This symmetry is of utmost importance in the operation of the coil.

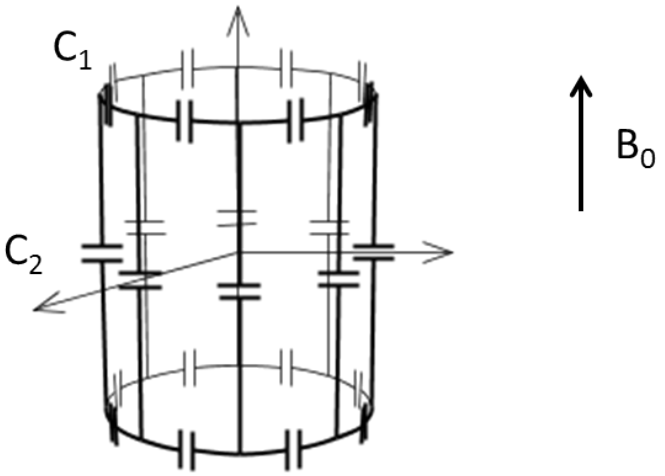


Figure 4.3: Scheme of the Birdcage coil with the direction of the main field indicated.

The resonant behavior of the Birdcage coil can be predicted quite simply using the transmission line model of the design, as shown in Figure 4.4. In this deduction the resistance of the conducting segments are neglected, however, this does not affect the resonant modes as they are independent from the resistance values as long as the discrete rotational symmetry is still valid. A detailed description that takes into account the resistance values can be found in [19].

We will start from Kirchhoff's mesh equations for the n-th mesh. We will denote the mutual inductances of two meshes in a distance of $n$ with $M_n$. Specifically, the self-inductance of a mesh is denoted with $M_0$. Note that since the two ends of the transmission line are connected and the whole line has N meshes, all indices are modulo N, that is, for example, $I_{n+N} = I_n$. Using these notations the mesh equation will be as follows:

$$\frac{2}{C_1}\int I_n \mathrm{d}t + \frac{1}{C_2}\int \left(I_n - I_{n-1}\right)\mathrm{d}t + \frac{1}{C_2}\int \left(I_n - I_{n+1}\right)\mathrm{d}t + \sum_{m=0}^{N-1} \frac{\mathrm{d}I_{n+m}}{\mathrm{d}t} M_m = 0 \qquad (4.2)$$

We carry this equation forward to frequency space with Laplace-transform:

$$2I_n\left(\frac{1}{C_1} + \frac{1}{C_2}\right) - \frac{1}{C_2}\left(I_{n-1} + I_{n+1}\right) + s^2 \sum_{m=0}^{N-1} I_{n+m} M_m = 0 \qquad (4.3)$$

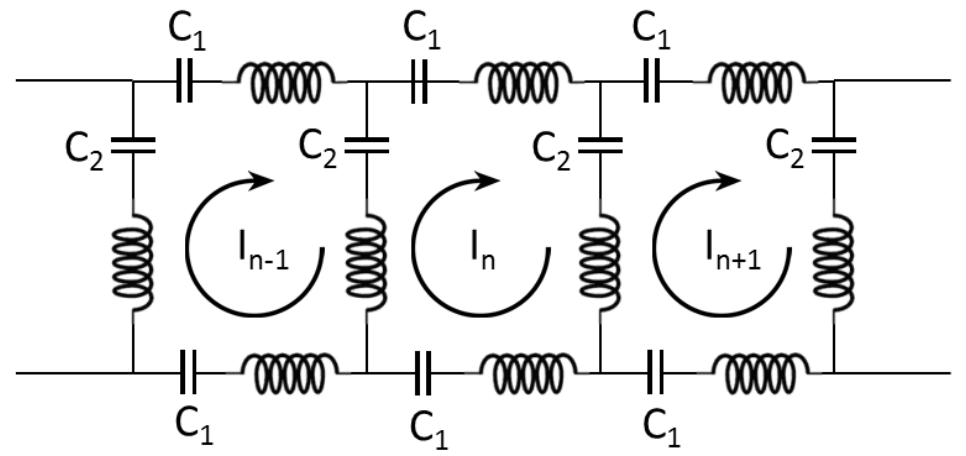


Figure 4.4: Section of the birdcage transmission line with the mesh currents. The left and right ends of the line are connected to each other.

The above (4.3) expresses a linear connection between the mesh currents, and therefore can be compressed to a matrix form:

$$\lambda \mathbf{M} \mathrm{I} = \mathbf{E} \mathrm{I} \tag{4.4}$$

With matrices $\mathbf{M}$ and $\mathbf{E}$ containing the inductance and capacitance parameters, I containing the Laplace transformed currents and $\lambda = s^2$.

The structure of the magnetic and electric matrices and the current vector in (4.4) can be read from the mesh equation (4.3):

$$\mathbf{M} = \begin{bmatrix} M_0 & M_1 & \cdots & M_{N-1} \\ M_{N-1} & M_0 & \dots & M_{N-2} \\ \vdots & \vdots & \ddots & \vdots \\ M_1 & M_2 & \cdots & M_0 \end{bmatrix}, \quad \mathrm{I} = \begin{bmatrix} I_0 \\ I_1 \\ \vdots \\ I_{N-1} \end{bmatrix} \tag{4.5}$$

$$\mathbf{E} = \begin{bmatrix} -2\left(\frac{1}{C_1}+\frac{1}{C_2}\right) & \frac{1}{C_2} & 0 & \cdots & \frac{1}{C_2} \\ \frac{1}{C_2} & -2\left(\frac{1}{C_1}+\frac{1}{C_2}\right) & \frac{1}{C_2} & \cdots & 0 \\ \vdots & \vdots & \ddots & \vdots & \vdots \\ \frac{1}{C_2} & 0 & \cdots & \frac{1}{C_2} & -2\left(\frac{1}{C_1}+\frac{1}{C_2}\right) \end{bmatrix} \tag{4.6}$$

As can be seen, both matrices are circulant, i. e. their n-th row is the first row circularly shifted by n-1. This property naturally occurs as the coil is made up of N identical meshes and the ends of the transmittion line are connected to each other.

From linear algebra we know that the elements of the eigenvectors of *any* circulant matrix are equal to the complex coefficients of the N-point Discrete Fourier Transformation. That is, the m-th element of the the k-th eigenvector $\mathrm{W^k}$ of such a matrix is the following:

$$\mathrm{W_m^k} = e^{-\mathrm{i}2\pi km/N} \tag{4.7}$$

These eigenvectors form an orthogonal basis of the N-dimensional complex vector space, therefore a circulant matrix can always be diagonalized with the matrix of the normed eigenvectors of the DFT components. Based on this fact we will write up the equation (4.4) with the diagonalized form of the matrices. We will denote the diagonal matrices by $\tilde{\mathbf{M}}$ and $\tilde{\mathbf{E}}$ and the matrix of the eigenvectors by $\mathbf{W}$.

$$\lambda \mathbf{W}\tilde{\mathbf{M}}\mathbf{W^{-1}}\mathrm{I} = \mathbf{W}\tilde{\mathbf{E}}\mathbf{W^{-1}}\mathrm{I} \tag{4.8}$$

$$\mathbf{W}\left(\lambda\tilde{\mathbf{M}} - \tilde{\mathbf{E}}\right)\mathbf{W^{-1}}\mathrm{I} = 0 \tag{4.9}$$

As can be seen, (4.9) is also an eigenvalue problem with the same solution: $\lambda = s^2 = -\omega^2$ for the resonance frequencies, and $\mathrm{I^k}$ for the current distributions.

The matrix we can see on the left side of (4.9) is the difference of two circulant matrices and hense is also circulant. Therefore, the eigenvalue solutions can be calculated easily. For an arbitrary circulant matrix with the first column vector A (the other columns are shifted versions of the first) the vector of eigenvalues $\tilde{\mathrm{A}}$ is given by the following expression:

$$\tilde{\mathrm{A}} = \mathbf{W}^T\mathrm{A} \tag{4.10}$$

In other words, the Discrete Fourier Transform of the elements of the first row or column. If we denote the eigenvalues of the magnetic matrix by $\tilde{\mathrm{M}}_\mathrm{k}$ and the ones of the electric matrix by $\tilde{\mathrm{E}}_\mathrm{k}$ (which are in the diagonals of matrices $\tilde{\mathbf{M}}$ and $\tilde{\mathbf{E}}$) then the solutions of (4.9) are the followings:

$$\lambda_k = \frac{\tilde{\mathrm{E}}_\mathrm{k}}{\tilde{\mathrm{M}}_\mathrm{k}} \tag{4.11}$$

$$\mathrm{I^k} \propto \mathrm{W^k} \tag{4.12}$$

That is, the possible current distributions at the resonant frequencies are proportional to the DFT vectors. Note that since the matrices $\mathbf{E}$ and $\mathbf{M}$ are symmetrical, the solutions are made up of degenerate solution pairs, that is, for any relevant $k$, $\lambda_k = \lambda_{N-k}$.

The fact that the solutions are the DFT vectors means that the physical current distributions associated to the real parts of the solutions in (4.12) are cosinusoidal (or sinusoidal - just a constant phase shift) around the coil with a $k$ number of cycles. As we mentioned in section 4, a sinusoidal current distribution on a cylindrical surface with one period per round produces a homogeneous transverse magnetic field inside the cylinder, so the solution with the index $k = 1$ is suitable for coil operation. However, with some calculations one can show that this $k = 1$ and its degenerate pair $k = N - 1$ are the only modes that produce a nonzero homogeneous magnetic field in the cylider [17].

Finally, we need to calculate the specific eigenvalues of matrices $\mathbf{E}$ and $\mathbf{M}$. In the following only the former is presented, because the latter can not be expressed simpler than the explicit DFT of the parameters $M_0, M_1$ etc. However, the computation of these parameters from the geometric properties of the coil can be found in Appendix A.

The eigenvalues of $\mathbf{E}$ can be calculated directly with the DFT elements. The first column vector of the matrix is denoted by E.

$$\tilde{\mathrm{E}}_\mathrm{k} = \mathrm{DFT(E)} = \sum_{m=0}^{N-1} E_m \mathrm{e}^{-\mathrm{i}2\pi km/N} = -2\left(\frac{1}{C_1} + \frac{1}{C_2}\right) + \frac{1}{C_2}\mathrm{e}^{-\mathrm{i}2\pi k/N} + \frac{1}{C_2}\mathrm{e}^{-\mathrm{i}2\pi k(N-1)/N} \tag{4.13}$$

The last exponential can be written in simpler form using the identity $\mathrm{e}^{-\mathrm{i}2\pi} = 1$:

$$\tilde{\mathrm{E}}_\mathrm{k} = -2\left(\frac{1}{C_1} + \frac{1}{C_2}\right) + \frac{1}{C_2}\mathrm{e}^{-\mathrm{i}2\pi k/N} + \frac{1}{C_2}\mathrm{e}^{\mathrm{i}2\pi k/N} \tag{4.14}$$

Finally, the two exponential terms may be combined to a cosine:

$$\tilde{\mathrm{E}}_\mathrm{k} = -2\left[\frac{1}{C_1} + \frac{1}{C_2}\left(1 - \cos\left(\frac{2\pi k}{N}\right)\right)\right] \tag{4.15}$$

Using this result and denoting tha magnetic eigenvalues simply by $\tilde{\mathrm{M}}_\mathrm{k}$ we finally get the resonance frequencies:

$$\omega_k = \sqrt{-\lambda_k} = \sqrt{-\frac{\tilde{\mathrm{E}}_\mathrm{k}}{\tilde{\mathrm{M}}_\mathrm{k}}} = \sqrt{\frac{2}{\tilde{M}_k}\left[\frac{1}{C_1} + \frac{1}{C_2}\left(1 - cos\left(\frac{2\pi k}{N}\right)\right)\right]} \tag{4.16}$$

Here $k$ indices the spatial frequency or wavenumber in cycles per round as the resonant frequencies are those at which the propagating wave has an integer number $k$ of wavelength around the structure. Therefore the spatial frequencies given in (4.16) can also be interpreted as a discrete dispersion relation for waves traveling in the coil.

Note that the birdcage coil has another resonant mode that cannot be expressed with mesh currents. This is when equal currents are flowing in the same direction in each

endring, and has a resonance frequency depending on the self- and mutual inductances of the endrings. Since this mode - referred to as co-rotating or CR mode - is not used in this thesis, nor in MR technology, the desription of this mode will not be detailed here.

Of course this simple thread I presented above can be also found in the literature, for example in [18], yet I personally find the local appearance of the Discrete Fourier Transform beautiful and I believe that the understanding of this concept can help to get a deeper insight to Fourier analysis, a tool used to describe an amazingly wide range of natural phenomena.

Now we got all the information needed to design, build and investigate the Birdcage coils for our imaging probehead. Given the results above we can predict the resonant behavior of the built coil from its capacitance and inductance parameters. The capacitance values of the used capacitors are of course given, the magnetic couplings can be calculated from the geometric parameters of the coil in the way described in Appendix A.

In practice however, Birdcage coils for proton are usually designed using the Birdcage Bouilder, a software by PennState Hershey College of Medicine [21]. This application is not only capable to predict the resonance frequencies in free air like the model described in above, but can also take into account that the coil is usually placed into a shielding tube that affects the RF operation and resonance frequencies. With this software, these effects can also be predicted and the coil can be designed right into the RF shielding. However, a disadvantage of this application is that it cannot design coils for arbitrary Larmor frequencies, only the ones the proton has in the commonly used magnetic field srengths.

Now we move on to the workflow of the coil construction and characterization, both for the coils built for Sodium and Hydrogen nuclei.

# 5. Construction and investigation of RF coils

In this chapter the detailed description of the work with the radiofrequency coils is presented. First the process of construction then the testing measurements are shown, including the resonance frequency check, the pulse length calibration and the measurement of $B_1$ homogeneity. These parts are described for both Sodium and Hydrogen coils.

## 5.1 Construction of $^{23}$Na and $^{1}$H coils

The first constructed coil was the one for Sodium nuclei. This decision was made due to the lower gyromagnetic ratio and thus the lower Larmor frequency of the Sodium nucleus. In our 7T system Sodium nucleus has the Larmor frequency of 79.4 MHz while the proton or Hydrogen nucleus has the one of approximately 300 Mhz. The latter is within the range of Ultrahigh Frequency (UHF) and therefore more problems seemed to arise when working with it previously in our lab. It was hence considered a good idea to get some experience with the Birdcage circuit in lower frequency first and then move on to the UHF version.

### Building the Sodium coil

The Birdcage coil built for Sodium nuclei was designed using the mathematical model of the Birdcage resonant frequencies described in section 4.1, the magnetic couplings were calculated with the method shown in Appendix A. However, these methods only predict the behavior of the system in the free air or vacuum, but of course in practice the coil is surrounded by metal parts, either of the NMR magnet itself or the RF shielding. The latter is a non-ferromagnetic metal tube in which the probehead is usually placed during the experiment to shield all high-frequency electromagnetic interactions that would adversely affect the coil operation. This shielding affects the coil operation usually by increasing the resonance frequency and changing the impedance matching. Hence Sodium has a gyromagnetic ratio different from the proton we could not use the Birdcage Builder [21] described in section 4.1 to calculate the effects of shielding. Therefore the only possibility was to design the coil to have a resonance frequency somewhat lower than the Larmor frequency of the Sodium nuclei, and hope that inside the magnet or the tube the shielding effect will increace its frequency to Larmor frequency. In the literature we found that an

appropriate RF shielding will increase the resonance frequency with about 15 - 20 % [18], therefore we designed the Sodium coil to have a frequency approximately this much lower than the Larmor of the Sodium.

The parameters and the calculated frequencies of the designed Sodium coil are shown in Figure 5.1. The highpass type was chosen for this coil where there are no capacitors dividing the legs, only between endring segments.

| Parameter | Value |
|---|---|
| Type | Highpass |
| Number of legs (N) | 6 |
| Diameter | 2.4 cm |
| Total height | 5.5 cm |
| Endring capacitance | 220 pF, SMD 1206, KEMET [23] |
| Leg capacitance | - (highpass coil, no leg capacitor) |
| Endring width | 4 mm |
| Leg width | 3 mm |
| Endring segment gap | 1 mm |
| Copper thickness | 250 µm |
| Holder | PVC tube |

| k (cycles per round) | $f_k = \omega_k / 2\pi$ [MHz] |
|---|---|
| 0 | 130.79 |
| **1** | **69.56** |
| 2 | 53.08 |
| 3 | 48.9 |

Figure 5.1: Physical parameters and calculated resonance frequencies for each wavenumber of the Sodium coil. The useful mode of wavenumber k=1 is highlighted with blue.

The coil was made up of 6 copper segments of a shape "I" fixed onto a cored PVC holder with superglue, leaving a gap between any two segments. For insulation checking the resistance between each neighbouring segment was measured by an Agilent U1732C Handheld LCR Meter. We found that the resistence is in the MΩ order of magnitude in each case. After that, capacitors of 220 pF were soldered to each gap. The data sheet of these capacitors is linked in [22]. These capacitors have a tolerance of 10 %, however for the coil building we measured the capacitance of each with the same LCR meter and used only the ones that have a value within 2 % of the nominal value. The used copper segments, the assembled layout and the built coil with the capaticors are shown in Figure 5.2.

For capacitor control we measured the capacitance between each segment after all the capatitors were soldered. We found that these capacitance values are all around 529 pF with a deviation of 3 pF. This justified that we used capacitors with proper values and all of them were properly soldered. This information is also useful in the case when one of the capacitors break due to mechanical damage as then the capacitance of the two given neighbouring segments will change (as well as the capacitance between all the others but

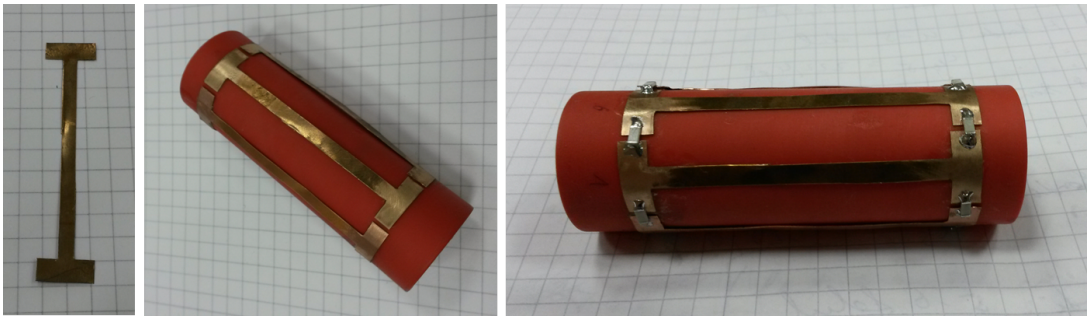

Figure 5.2: Left: one of the six copper segments of the coil. Middle: All the segments fixed onto a PVC holder with a gap between each. Right: The built coil with all the capacitors soldered.

those will show less alteration). In this way we can determine which capacitor needs to be changed with simple capacitance measurements.

After that we have fastened our coil to a probehead frame previously built by Anita Karsa [23]. With this frame the coil could be placed inside the magnet and can be driven through an SMD plug. The frame is made up of copper rods and PVC discs for mechanical stability. For impedance matching we used a non-magnetic trimmer capacitor in series between the signal and the end of one of the segments. The scheme of the circuit and the probehead frame with our coil and the trimmer capacitor is shown in Figure 5.3. Note that as can be seen in this figure we used both of our coils in linear mode thus creating linearly polarized $B_1$ fields. We did this because we did not have the required 90° RF hybrid circuit for quadrature drive.

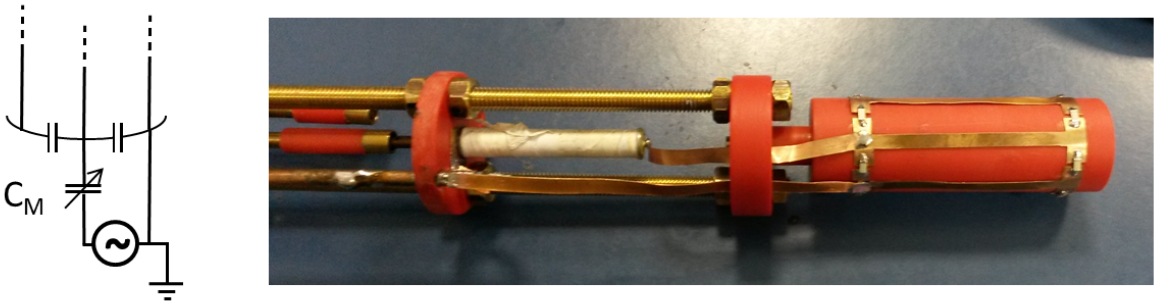


Figure 5.3: Left: scheme of the Birdcage and the impedance mathing trimmer capacitor. Right: Probehead frame built by Anita Karsa [23] with our coil and the trimmer capacitor (white) fastened on it.

The whole probehead with the coil, the trimmer capacitor and the SMD plug is shown in Figure 5.4.

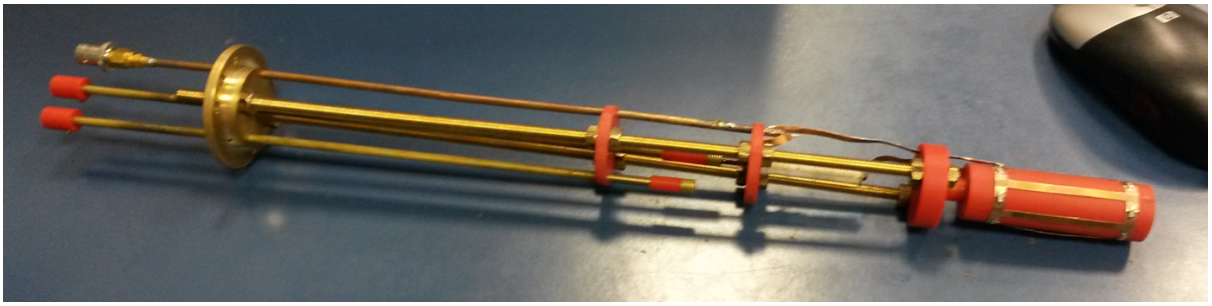

Figure 5.4: The whole probehead with the frame, the Sodium Birdcage coil and the trimmer capacitor. The SMD plug is at the bottom of the probehead on the left.

## Building the proton coil

The construction of the proton coil was somewhat different than of the Sodium. First, PVC contains Hydrigen so it is not suitable for the coil holder, instead we used Polytetrafluoroethylene often referred to as Teflon of PTFE for mechanical mounting. Second, in this time the conducting parts of the coil were made out of adhesive copper foil with a thickness of 50 µm. Furthermore, this time we could use both the Birdcage model described earlier and the Birdcage Builder software as we designed this coil for proton in a commonly used 7T system. For the proton coil we chose the bandpass design where both the endrings and the legs are divided by capacitors.

In our first coil we used 22 pF capacitors in the endrings and 18 pF capacitors in the legs as these were the closest values to what the Birdcage Builder gave us for 300 MHz and without the use of the shielding tube, in a case where only the NMR magnet behaves as shielding. However, we found that in this way the resonant frequency of the appropriate resonant mode will be too high when the probehead is inside the magnet as it was about 306 MHz. This small difference in the resonance frequency is a major problem as the Birdcage coil is not a tuneable design. As the capacitance values are given, the only possibility remains is that we estimated the magnetic couplings a bit imperfectly. Therefore, we got the formula of the Birdcage resonance frequencies in (4.16), substitute our capacitance values in it and make it equal to 306 MHz in the $k = 1$ case. From this we could reestimate the $\tilde{M}_k$ magnetic couplings from which we could determine the needed capacitance values for a resonant frequency of 300 MHz. We got that the exact needed capacitance value is 21.14 pF. Since we did not have the exact value we used the same 22 pF capacitors both in the legs and the endrings. According to the formula this would result a resonance frequency of 298.6 MHz which is much closer to the desired 300 MHz than the original 306 MHz. In the followings we describe this version where all the capacitors were of 22 pF.

The physical parameters of this proton coil and the resonance frequencies in air calculated with our Birdcage model are shown in Figure 5.5.

| Parameter | Value |
|---|---|
| Type | Bandpass |
| Number of legs (N) | 8 |
| Diameter | 2.4 cm |
| Total height | 6.4 cm |
| Endring capacitance | 22 pF, SMD 1206, KEMET [23] |
| Leg capacitance | 22 pF, SMD 1206, KEMET [23] |
| Endring width | 4 mm |
| Leg width | 2 mm |
| Endring segment gap | 1 mm |
| Copper foil thickness | 50 µm |
| Holder | Teflon (PTFE) tube |

| k (cycles per round) | $f_k = \omega_k / 2\pi$ [MHz] |
|---|---|
| 0 | 476.98 |
| **1** | **268.92** |
| 2 | 244.16 |
| 3 | 241.88 |
| 4 | 242.18 |

Figure 5.5: Physical parameters and calculated resonance frequencies for each wavenumber of the proton coil. The useful mode of wavenumber k=1 is highlighted with blue.

In this case first the adhesive copper coil was cut and glued to the Teflon tube in the suitable way. After that the capacitors were soldered and fixed with superglue. The capacitors were tested one by one in order to reduce the tolerance of the used capacitance values to 2 % just like at the Sodium coil. The insulation check was done in the same way and with the same result as in the case of the Sodium coil. The capacitance check was also done in the two sides of every capacitor. The capacitance values were between 40.5 and 42.5 pF between the two sides of any leg capacitor, and between 36 and 38 pF between the two sides of any endring capacitor. Because of the imperfect cunductance of the copper foil adhesive the connections between foils were also soldered to each other.

The Teflon holder with the sticked foils and the completed coil are shown in Figure 5.6.

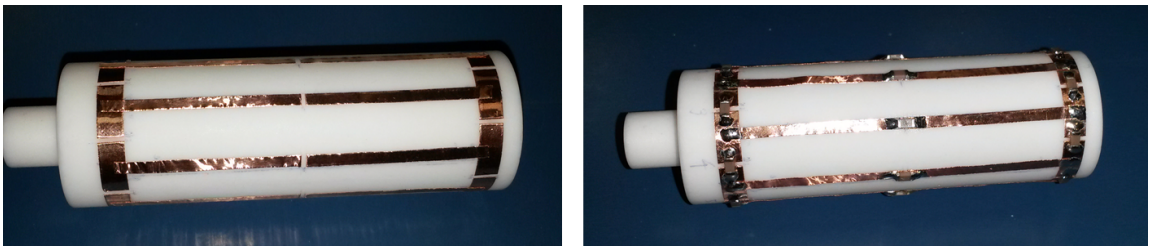

Figure 5.6: Left: Teflon holder with all the copper foils fixed to it. Right: Completed proton Birdcage coil.

Thereafter the coil was fixed onto the same probehead frame with the same trimmer capacitor as the Sodium coil. The fastening of the coils was made in such a way that the

coils could be changed easily without alternations on the probehead frame, making sure that the two coils are placed in the same position inside the magnet. The proton coil on the probehead is shown in Figure 5.7.

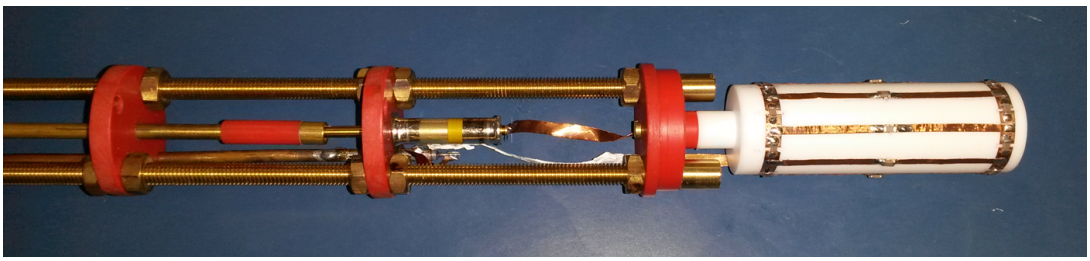

Figure 5.7: Probehead with the proton Birdcage coil fixed to it.

I seize the opportunity here to compare our Birdcage model with the widely used Birdcage Builder software. If we set the latter to design a coil with the same geometrical parameters as our coil with 22 pF leg capacitors to 300.52 MHz at 7T without shielding we got that the endring capacitors need to be the value of 17.08 pF. If we put these capacitance values and the same geometry to our model implemented in Matlab, it says that such a coil will have a resonant frequency 297.376 MHz in air. This means that our model is capable to predict the unshielded resonance frequencies with a high accuracy as it provides a result that is only 1.06 % different from the one given by the commercially used software.

## 5.2 Checking resonance frequencies

After the coils were built and fixed to the probehead frame their resonance frequencies were checked using the NMR spectrometer's wobble function. This means we swept a wide range of frequencies with the signal and measured the signal reflection as a function of frequency. As commonly known, a resonator will have a sharp minimum of its reflection when the frequency of the signal equals to the resonance frequency of the circuit. Therefore by observing the minimums in the frequency-dependent reflection, also called the wobble curve, we are able to determine the resonance frequencies of the given circuit.

In our case these measurement consisted of two parts for both coil. First we checked whether our model predicted the resonance frequencies in air correctly. In this part the coils were measured outside the magnet with a wide frequency range to observe as many resonant modes as possible. Thereafter we put the probehead into the magnet and measured the resonance frequency of the only mode ($k = 1$) useful for us inside the magnet. In this time we only swept the signal frequency in a range of a few MHz's as we are

interested in the exact resonance frequency of only one mode. We also checked if we can match the impedance of our circuit to 50 Ω to minimize signal reflection at the given frequency.

## Resonance frequencies of the Sodium coil

The wobble curve measured with the coil outside the magnet and the calculated resonance frequencies are shown in Figure 5.8. We have marked the measured and the calculated frequencies of each mode on the wobble curve for easier comparison.

Calculated frequencies:

| k | 0 | 1 | 2 | 3 |
|---|---|---|---|---|
| $f_k = \omega_k/2\pi$ [MHz] | 130.79 | 69.56 | 53.08 | 48.90 |

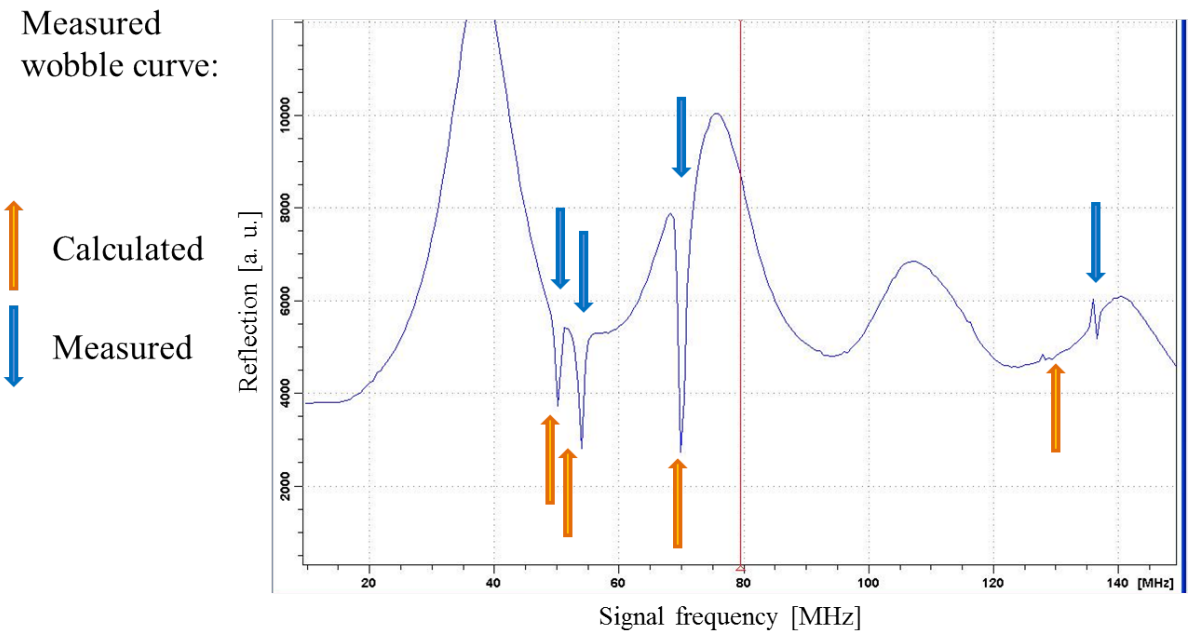


Figure 5.8: Calculated resonance frequencies and the measured wobble curve with the Sodium coil outside of the magnet. Observeable minimums are marked with blue arrows for better recognizability, calculated frequencies are marked with orange arrows for easier comparison.

As can be seen the resonant frequencies in air are well predicted except the one of the mode $k = 0$.

After that we put the probehead with the Sodium coil into the magnet and performed another wobble experiment with a narrow frequency range around Sodium Larmor frequency 79.4 MHz. As we have mentioned it before, we designed the coil to have a resonance

frequency somewhat lower than this in air in order to reach the Larmor frequency inside the magnet. Therefore, we could only hope that inside we would approach the desired 79.4 MHz. The wobble curve is shown on Figure 5.9.

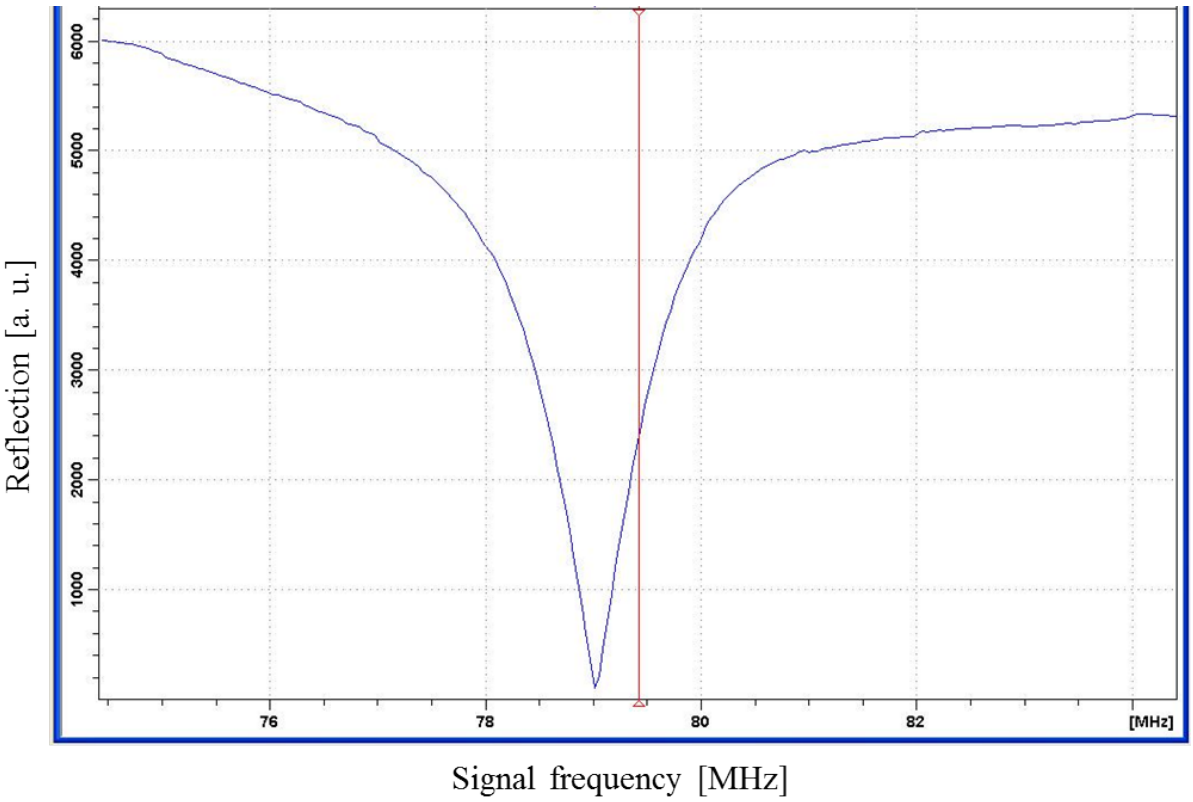


Figure 5.9: Wobble curve of sodium coil inside the magnet. Vertical red line marks the Larmor frequency of Sodium.

As can be seen we did not reach the exact Larmor frequency marked with red vertical line. As mentioned before, this difference is not neglectible since the Birdcage coil is not a tuneable design. The problem was solved quite haphazardly. We found an unused Teflon tube in the lab with a copper ring on the bottom of it shown in Figure 5.10. There are some examples in the literature where a Birdcage coil is tuned by adding an additional conducting ring around it that affects the inductive couplings in the system, increasing the resonance frequencies (behaving like an additional shielding). We simply pulled this tube over our coil, and retried the wobble experiment. The result shown in Figure 5.11 is surprisingly fine.

However, these measurement were made without any sample, nonetheless a sample can modify the tuning and matching. Therefore the wobble measurement was repeated with the coil filled with 1 Mol aqueous solution of salt. In this case with a little setting of the screws that fix the probehead into the magnet we could achieve a same result as

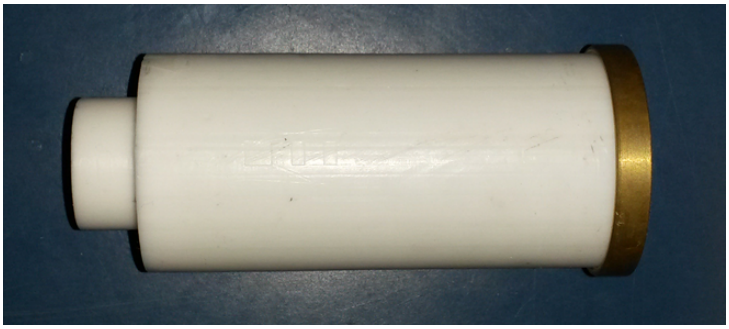

Figure 5.10: Teflon tube with a copper ring on it used to tune the Sodium coil.

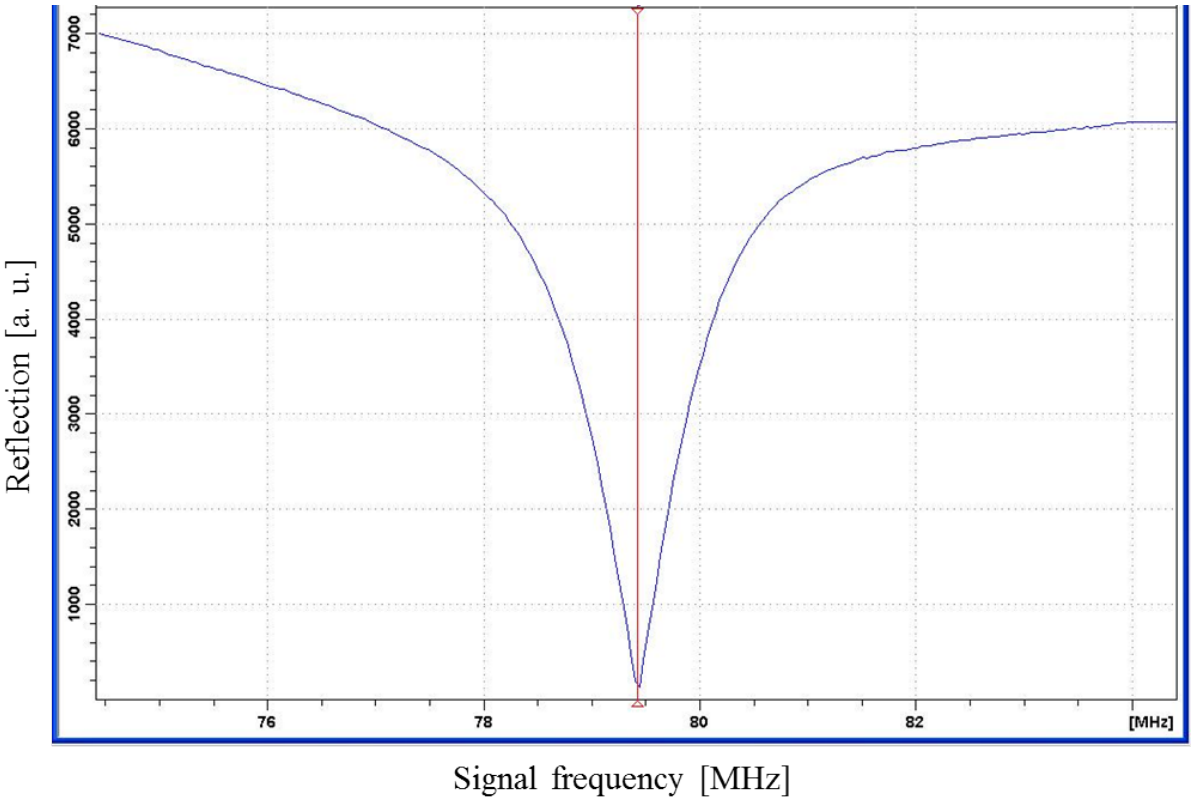


Figure 5.11: Wobble curve of Sodium coil inside the magnet with the Teflon tube with the copper ring pulled on.

the one in Figure 5.11. The observation that by adjusting the fixing screws the resonance frequency can be modified within a range of tenth of percents was used heavily for the proton coil.

Both the results in Figure 5.9 and 5.11 are obtained after adjusting the trimmer capacitor on the probehead, or in other words, both are matched results. This was done in order to minimize signal reflection by setting the impedance of the circle as close to $50\,\Omega$ as possible. In MR technology, signal reflection is usually expressed in decibels as follows:

$$R[dB] = 20\log\left(\frac{U_{refl}}{U_{in}}\right) = 10\log\left(\frac{P_{refl}}{P_{in}}\right) \tag{5.1}$$

In imaging processes the rule of thumb is the reflection to be below -15 dB. From results shown in Figure 5.9 and 5.11 one can calculate that we achieved a reflection of about -30 dB in this case, which is excellent. Although we were not always able to reach this value, the reflection was always well below -20 dB in our experiments.

## Resonance frequencies of the proton coil

For the proton coil the resonance frequency chech was done in the exact same way. The wobble curve measured with the coil outside the magnet and the calculated frequencies are shown in Figure 5.12. The frequency according to $k = 0$ is too high for our amplifier and therefore this mode was not measured.

Calculated frequencies:

| k | 0 | 1 | 2 | 3 | 4 |
|---|---|---|---|---|---|
| $f_k = \omega_k/2\pi$ [MHz] | 476.98 | 268.92 | 244.16 | 241.88 | 242.28 |

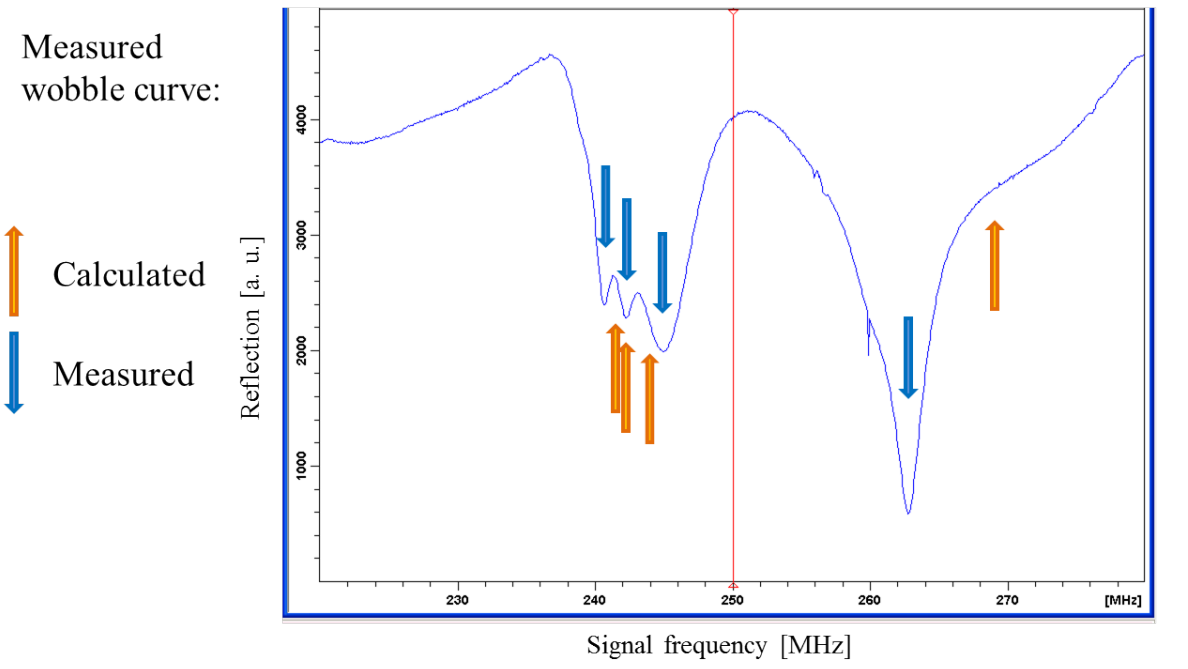


Figure 5.12: Calculated resonance frequencies and the measured wobble curve with the proton coil outside of the magnet. Observeable minimums are marked with blue arrows for better recognizability, calculated frequencies are marked with orange arrows for easier comparison.

As can be seen, the resonance frequencies are quite well predicted except the $k = 1$ one where there is an error of about 2.5 %. After this we put the probehead with the proton coil inside the magnet and obtained another wobble curve with a narrow frequency range. The result is shown in Figure 5.13.

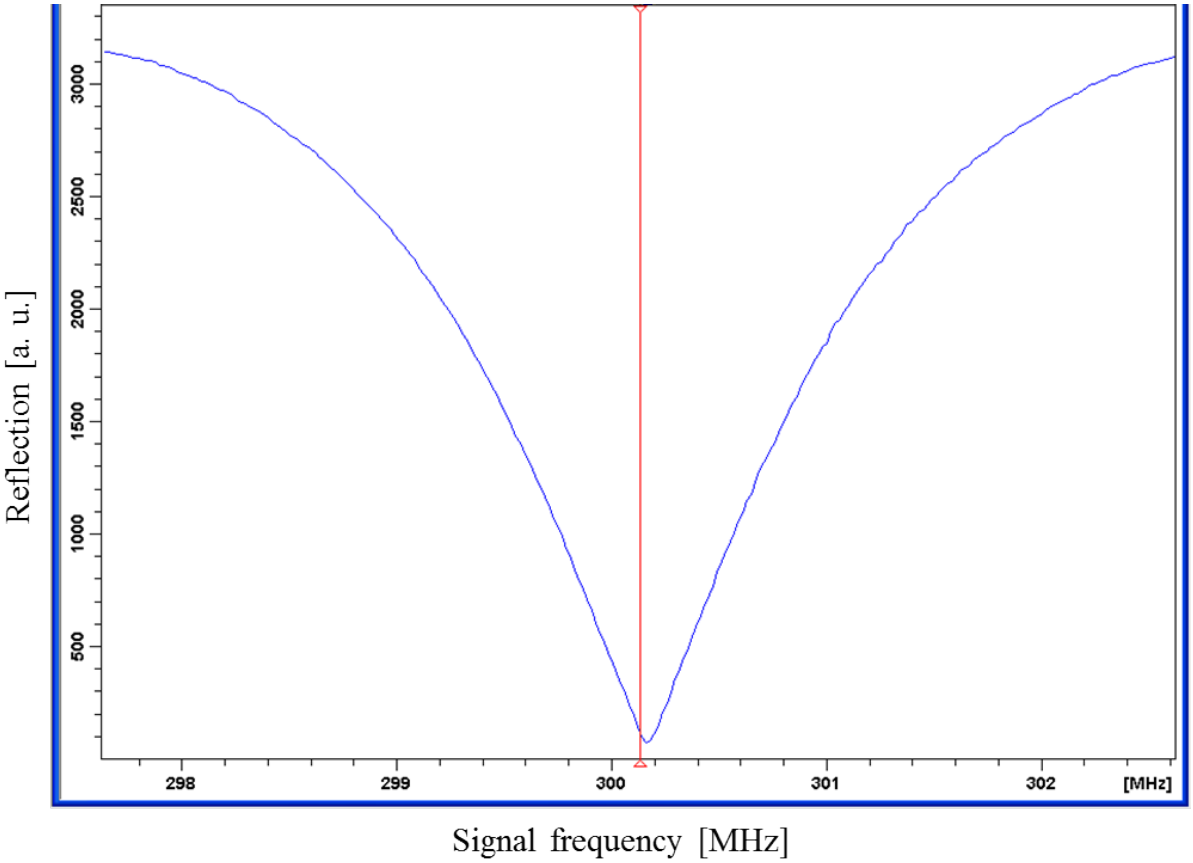


Figure 5.13: Wobble curve of proton coil inside the magnet. Vertical red line marks the Larmor frequency of the proton.

In this case the reflection is about -25 dB, and the resonance frequency is somewhat differs from Larmor, but we found that such a small difference does not affect the measurements, and if still does, then can be easily corrected by adjusting the fixing screws. This experiment was also repeated with water samples in the coil, resulting quite similar. In some cases when the sample was large or when the gradient coils were already on the probehead we heavily used the adjustment of the probehead fixing screws as a method of tuning the circuit. In this way the proton coil could be tuned in a range of 1-2 MHz's.

## 5.3 Pulse length calibration

In order to perform NMR or MRI experiments we need to control the excitation, in other words, we have to know how the spins are affected by a radiofrequency pulse of a certain length. As mentioned at the end of section 2.2 an RF field oscillating with Larmor frequency can turn the spins in the rotating reference frame with an angle determined by the formula (2.30). As a reminder, the angle is the following:

$$\Delta\theta = \gamma b_1 \tau \tag{5.2}$$

As described at the signal detection part we can only measure the transverse component of the magnetization which can be calculated with the sine of the angle between the magnetization and the $z$ axis, i. e. the sine of $\Delta\theta$ in the above equation. Therefore with a given RF field strength $b_1$ our signal $S$ depends on the pulse length $\tau$ as follows:

$$S \propto M_\perp \propto \sin(\Delta\theta) = \sin(\gamma b_1 \tau) \tag{5.3}$$

This phenomenon that the NMR signal sinusoidally depends on the pulse length is called Rabi oscillation [24].

To determine the pulse length needed for excitation of a certain angle we performed an experiment to measure this Rabi oscillation. That is, we measured the signal as a function of pulse lenght and observed the sinusoidal dependence. With such data one can easily calculate the needed pulse length for every excitation angle.

### Pulse lengths of the Sodium coil

For the Sodium coil we measured the NMR signal of 1 Mol aqueous solution of salt. The sample geometry was cylindrical with a height of 15 mm and a diameter of 10 mm, therefore containing 1178 µl sample. The pulse length was swept from 25 µs to 1750 µs with a step interval of 25 µs. The pulse sequence was a simple FID experiment, the signal was considered to be the integral of the absolute value of the FID after a baseline correction multiplied by the sign of the real part of the FID. In this way the noise can be eliminated as it has zero mean value after the baseline correction. The result is shown in Figure 5.14.

With simple Fourier analysis the frequency of the sine in Figure 5.14 is 1328.125 Hz, from which the pulse length needed for an excitation of 90° is 188.2 µs.

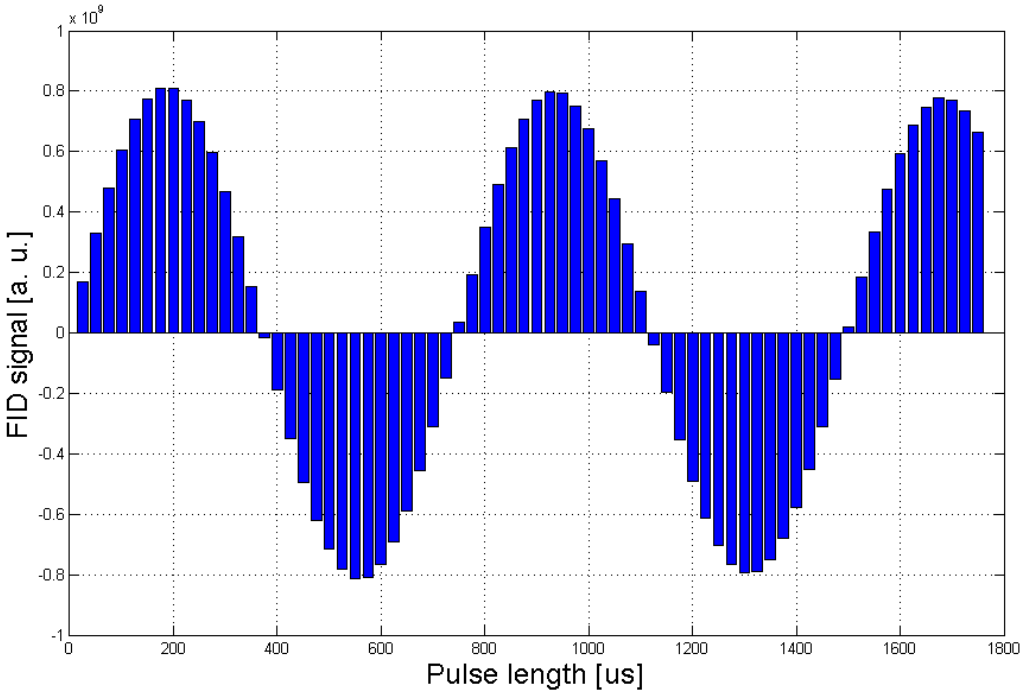


Figure 5.14: NMR signal of 1178 µl salt solution sample with Sodium Birdcage coil as a function of pulse length.

## Pulse lengths of the proton coil

The pulse length calibration for the proton coil was done with the same method. This time the sample was somewhat bigger with a height of 18 mm and the diameter of 12 mm in a cylindrical geometry, therefore consisted 2036 µl of distilled water. This time we swept the pulse length from 15 µs to 1050 µs with steps of 15 µs. The NMR signal is also given here by the integral of the FID just like in the case of the Sodium coil, for the same reasons. The result is shown in Figure 5.15.

With a same Fourier analysis one can obtain that the frequency of the sine is 2148.44 Hz, from which the pulse length of a 90° excitation is 116.4 µs. The difference between the Sodium and the proton pulse length is due to three factors: their gyromagnetic ratio, the amplitude of the transverse field produced by the coil with unit current, i. e. the RF coil efficiency, and the differences of the signal amplifiers used for Sodium and proton.

## Remark

It is important to notice that performing the excitation at the exact Larmor frequency is of utmost importance in this experiment. In both of the experiments presented above the excitation frequency was equal to the Larmor frequency within a tolerance range

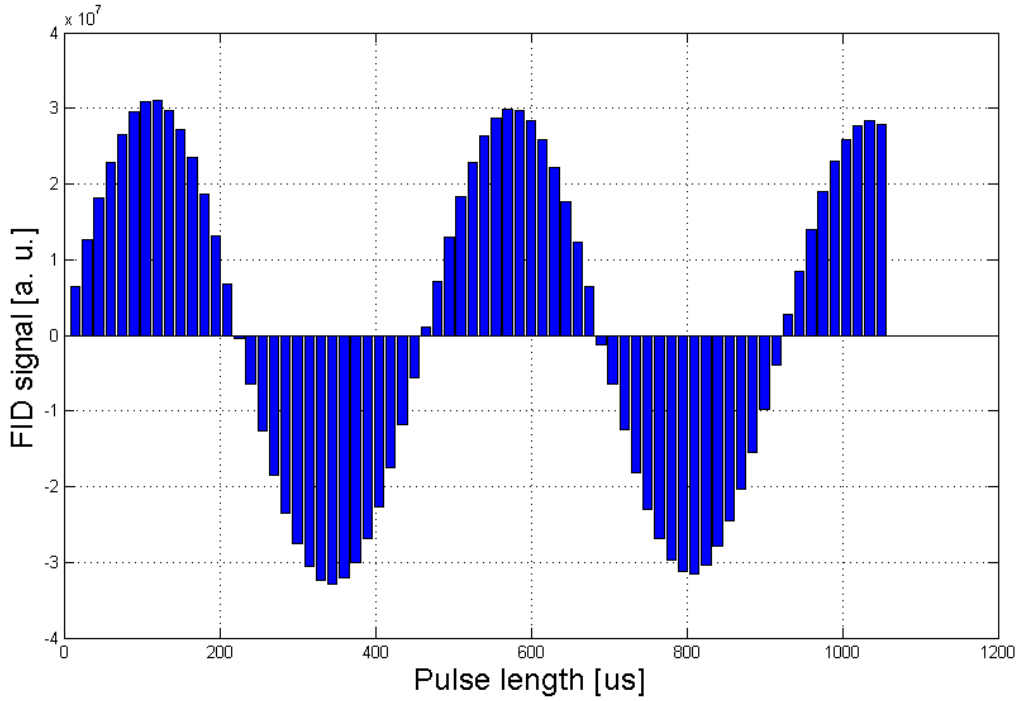


Figure 5.15: NMR signal of 2036 µl water sample with proton Birdcage coil as a function of pulse length.

of ± 10 Hz. To demonstrate the consequences of deviations from Larmor frequency we performed another experiment with the Sodium coil where the excitation frequency was intentionally shifted by 300 Hz which equals to 3.78 ppm. In this case the rotating coordinate system has a different angular frequency than the rotating spins, therefore nonzero rotation of the spins could be experienced even in the rotating frame. Consequently, our excitation will be imperfect due to the off-resonance condition, i. e. the term $(\omega - \omega_0)$ in (2.27) will be nonzero, so our spins will not simply turn around the $x'$ axis of the rotating frame but will have a rather complicated trajectory during the excitation. This means that the sinusoidal depencende of the signal from the pulse length is no longer valid, therefore the pulse length calibration will give a false result. This effect increases with the pulse length so it can be neglectable for common excitations of 90° and 180° but becomes significant in larger angles and pulse lengths.

Another disadvantage of the frequency offset that the signal demodulation is incomplete, meaning the FID signal is oscillating. This can be demodulated manually during the data processing, but we will not be able to determine the sign of the FID signal since the imperfect excitation leads to a phase shift in the signal that intricately depends from the pulse length. Hence we can only determine the absolute value of the FID signal. This is shown in Figure 5.16. The aberration of the Rabi oscillation is clearly observable.

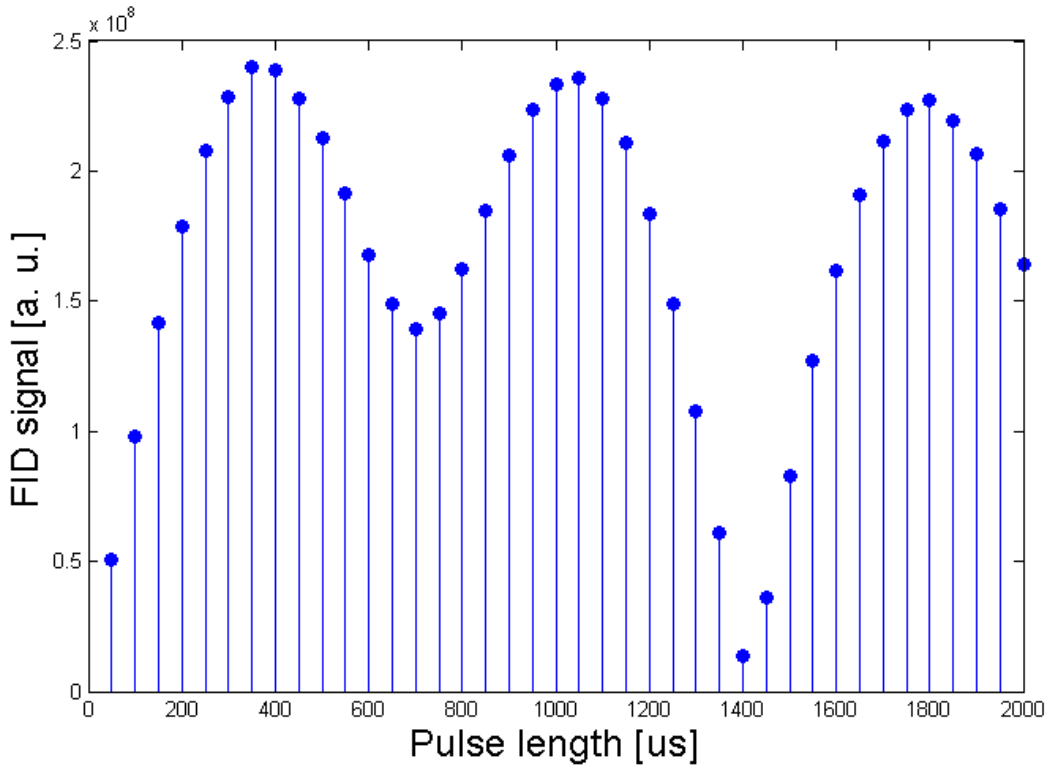


Figure 5.16: Absolute value of NMR signal as a function of pulse length on salt solution sample. The excitation frequency is purposely shifted from the Larmor frequency to show the consequences of the off-resonance condition.

## 5.4 Measurement of $B_1$ field homogeneity

To perform more complicated pulse sequences with severe excitations we have to ensure that the pulse length needed for a certain angle is approximately the same in the whole sample volume, that is, the produced $B_1$ field is homogeneous enough. The first method to measure $B_1$ homogeneity uses the information provided by the Rabi oscillation. If the RF field is perfectly homogeneous in the sample volume the NMR signal has an exact sinusoidal shape (we now neglect the effect of $T_2$ relaxation during the excitation as the characteristic time $T_2$ is 30× greater than longest the pulse at Sodium and 1000× greater at proton). However if the field is inhomogeneous in the sample volume the spins in various parts of the sample will be rotated with a different angle, therefore the net magnetization will decrease. This effect becomes more significant as the pulse length increases, causing the envelope of the Rabi oscillation curve to decrease. This reduction exist in both of the measured data shown in Figures 5.14 and 5.15, although it s more observable in the case of the proton coil where the sample volume was larger.

It is a rule of thumb in this topic that if the amplitude of the NMR signal after an excitation of 810° is at least 70 % of the signal acquired after a 90° pulse then the RF field is sufficiently homogeneous in the sample volume [25]. In our experiments we measured the amplitudes as the maximal signal value in the fifth and the first "half-wave" of the sines.

In the case of the Sodium coil this ratio is comparable to the $T_2$ decay in this time interval, telling us that the produced $B_1$ field shows excellent homogeneity in this cylindrical sample volume of height 15 mm and diameter 10 mm:

$$\left[\frac{S(810°)}{S(90°)}\right]_{\mathrm{Na}} = 95.5\% \tag{5.4}$$

The Rabi oscillation measured with the proton coil on water sample shows a greater reduction, but is also far above the compliance limit:

$$\left[\frac{S(810°)}{S(90°)}\right]_{\mathrm{H}} = 79.5\% \tag{5.5}$$

That means the the proton coil also provides a sufficiently homogeneous RF field in the cylindrical volume of height 18 mm and diameter 12 mm.

## $B_1$ mapping in the Sodium coil

There is another method to measure the radiofrequency field homogeneity that provides more information of the field distribution called $B_1$ mapping. This means that we use a little sample in different positions inside the coil and measure the pulse length needed for a certain excitation angle, from which the field amplitude can be calculated using the excitation angle formula in (2.30):

$$b_1 = \frac{\Delta\theta}{\gamma\tau} \tag{5.6}$$

For metrology reasons one should measure the pulse length of an angle where the Rabi oscillation curve is steep, like 180°. In this way if we have an error in the signal amplitude it will cause a little error in the calculation of the needed pulse length. If we measure the pulse where the curve is flat like at 90° then a little mistake in the signal amplitude will cause a great error in the calculated length. Mathematically this can be expressed as the problem is well conditioned if we measure where the Rabi curve is steep [26].

The measurement procedure with the Sodium coil was the following. We got a cylindrical sample of height and diameter of 4 mm consisting about 50 µl 1 Mol salt solution, and put it into 9 different positions along the axis of the coil. In every position we measured the FID signal with numerous pulse length around the 180° excitation. In this

region the sine of the Rabi curve can be approximated linearly as the next element in its series expansion is zero. Therefore as we measured near to the 180° we could fit a linear curve to the points whose zero-section determines the exact pulse length needed for a 180° excitation, from which the $B_1$ field is easily calculated using (5.6). The signal value was determined as the integral of the FID after baseline correction with the same method as the Rabi oscillation measurements.

In Figure 5.17 one of the measured position and the calculated $B_1$ field values are shown. It can be seen that in the central 4 cm of the coil the field value variates less than ±5%. On the right, the effective value of the field is shown as our coil produces linearly polarized transverse field, therefore the spins rotate as it was a circular field with a half amplitude as we have seen in (2.24).

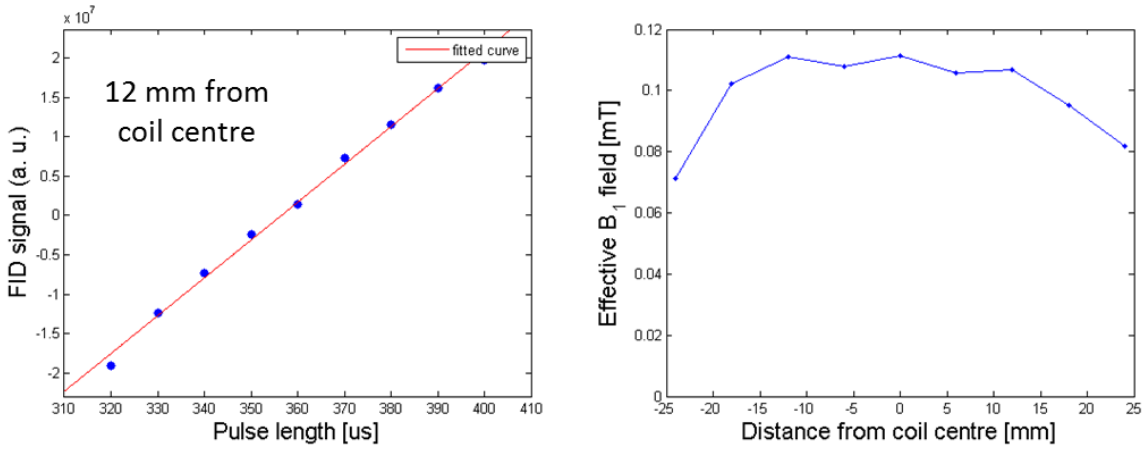


Figure 5.17: Left: FID signal vs. pulse length around the 180° excitation with the sample on the coil axis, 12 mm from coil centre and the fitted linear curve. Right: Calculated effective RF field in different positions on the coil axis.

This method unfortunately was only applicable to the Sodium coil because of the background signal of the proton coil. In essence, even if measured without sample the proton coil gives a signal small enough to be neglected in an NMR or MRI measurement but large enough to be comparable of the signal achieved with nearly 180° excitation of a small sample. The amplitude and time course of this background signal was even dependent of the pulse length making it impossible to perform a similar measurement on the proton coil. Of course this could have been done using much bigger samples or measuring near the 90° pulse, but the first would highly reduce the resolution of the mapping and the second would strongly amplify the error in the calculated field as the problem becomes poorly conditioned. Because of these reasons we decided not to perform a similar mapping in the proton coil hence we already know from the Rabi oscillation that the homogeneity of the coil is suitable in the desired sample volume.

# Part II

# The gradient system

# 6. General description of gradient fields in MRI

As we have seen in section 2.6 the imaging process requires the magnetic field to vary in space linearly as the diferent Larmor frequencies will encode the location of the spins. In this chapter a brief overview of the gradient field theory is presented, including the desired optimal fields and also the conceptual obstacles that limit the availability of such fields.

To get started, we repeatedly mention that although its magnitude can and does vary in space and time, the desired optimal gradient field is always parallel to the main static field $\mathbf{B_0}$ and does not have a transverse component which would be perpendicular to the static field. (Note that we do not talk about the RF field now, only the main field and the gradients.)

Therefore the field can be expressed in the following way, with the main field parallel to the $z$ axis of the coordinate system:

$$\mathbf{B}(\mathbf{r},t) = (0,0,B(\mathbf{r},t)) \tag{6.1}$$

We would like to have such a field that varies in space linearly, but the magnitude of the variaton, i. e. the gradient strength can also change in time as we switch gradients on and off in an imaging experiment. When expressing it mathematically, we want the only nonzero component of the field to be the following:

$$B(\mathbf{r},t) = B_0 + \mathbf{G}(t)\mathbf{r} = B_0 + G_x(t)x + G_y(t)y + G_z(t)z \tag{6.2}$$

In (6.2) the vector $\mathbf{G}$ is called the gradient, as it really is the gradient of the $z$ component of the magnetic field. An example of the $x$ gradient is shown in Figure 6.1.

Unfortunately there is a serious problem with this concept: Maxwell's equations forbid the existance of a field described in (6.1) and (6.2). Specifically the existance of the $z$ component of the gradient violates the condition $\nabla\mathbf{B} = 0$ as an above field have a divergence equal to $G_z$ while the other two components of the gradient contradict the equation $\nabla \times \mathbf{B} = \mu\left(\mathbf{J} + \varepsilon\frac{\partial \mathbf{E}}{\partial t}\right)$. Note that although theoretically the needed rotation could be achieved by suitable currents and time-varying electric fields, in practice non of them can exist as the sample or the patient does not conduct well enough for the necessary current; and in the stationary solution when the gradient is constant in time the absence of time-varying magnetic field exludes the existance of an appropriate electric field.

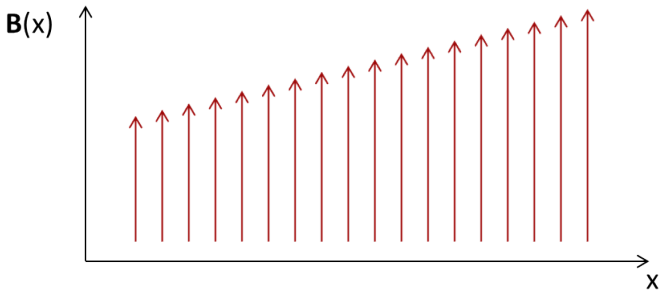


Figure 6.1: Illustration of the $x$ gradient field. Note that the gradient vector points to the $x$ direction but the field only has $z$ component.

All in all, the laws of electromagnetism prohibits a field whose variation in space is perfectly linear. What can be done is to eliminate as many terms other than linear in the series expansion of the magnetic field as possible.

However, there is another problem to take into account. Also due to Maxwell's equations if the magnetic fields vary in space then it must have transverse components as well. Fortunately these components are small enough compared to the main field and to the $z$ component of the gradient, therefore their effect is usually neglectable [6].

After this short summary of gradient field theory we now move on to the practical realization of these gradients, i. e. to the gradient coils.

# 7. Gradient coils in MRI

According to what we have previously seen, the method of magnetic resonance imaging fully relies on linearly varying magnetic fields; nevertheless, producing a field that approximates a perfectly linear gradient described in (6.2) as close as possible is clearly not trivial. The basic concept is having a coil that creates a magnetic field that varies more or less linearly in a certain direction, but the specific coil types are and will be subjects of development. The difficulty of the task is supported by the fact that designing better and better gradient coils has become a profession itself.

It is not a purpose in this thesis to provide a deep insight to gradient coil designs, we will focus only on the two basic coil types that were constructed as part of the built imaging probehead, the Maxwell pair and the Golay coil. These designs were chosen to our probehead because they are relatively simple to construct yet they produce a gradient field good enough.

But what would we consider as a good field? The gradient field goodness considerations follow directly from the imaging requirements. We want a coil and a field that:

- As linear as possible, i. e. many nonlinear terms vanish in the series expansion of the field
- Has a homogeneous gradient in a large volume, that is, a volume where the spatial derivative of the field remains almost constant. The tipical measurement of this is the Diameter of Spherical Volume (DSV) that describes the maximal volume where the variation of the gradient is less than 5 %.
- Has a good efficiency, which means that it produces a large gradient value with unit current flowing through the coil. The definition is simply the ratio of the gradient strength and the current: $\eta \equiv \frac{G}{I}$.
- In MRI technique it also a point that we would like to switch the gradient field on and off as fast as possible. This requires the self-inductance of the gradient coil to be low, and the power supply to be fast. A high coil efficiency can also help as then we do not need large current values to produce the desired gradient.

In the following sections we present the two gradient coil designs chosen for our imaging probehead followed by the detailed workflow of the construction of the coils and the investigation of their characteristics.

## 7.1 The Maxwell pair

First we show the basic design of a coil that produces gradient parallel to the main field, also referred to as $z$ gradient. This coil has its name after Maxwell and it can be said that this is the optimized version of the simplest coil one can imagine.

The design of the coil is shown in Figure 7.1. As can be seen the layout is made up of two circular conductive loop that carry currents of the same magnitude and the opposite direction.

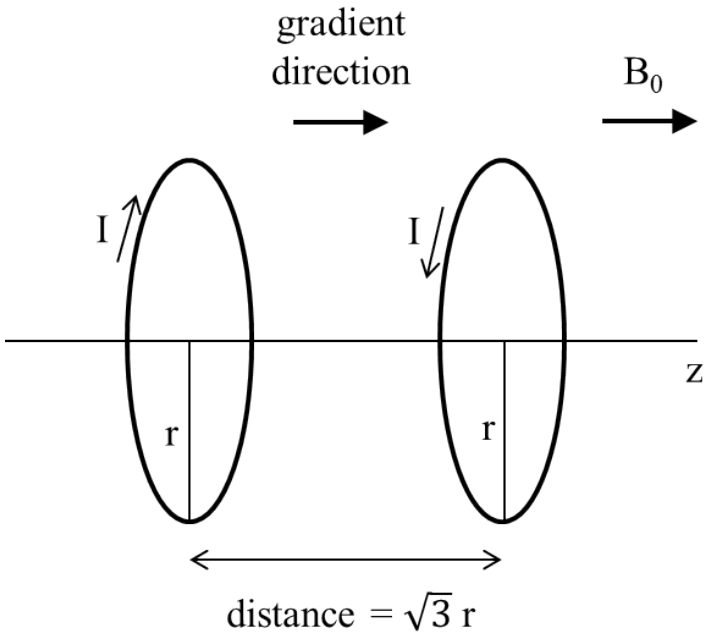


Figure 7.1: Maxwell design as a simple $z$ gradient coil.

With a coil design antisymmetric in the $z$ direction like in this case, the even powers of $z$ are all zero in the series expansion of the field. The only parameter to be optimized is the ratio of the radius and the distance of the loops. With simple calculation one can found that if this ratio equals to $\sqrt{3}$ then the $z^3$ term can also be eliminated, so the first nonzero nonlinear term will be $z^5$ which results in a reasonably homogeneous gradient field.

Thanks to the simple coil design the calculation of the produced gradient field is straightforward, from which one can obtain that the characteristic quantity of the gradient homogeneity, the Diameter of Spherical Volume of this coil is approximately equals to the loop radius $r$, while the coil efficiency is approximately $\eta = 0.66\frac{\mu_0}{r^2} = \frac{8.058\times10^{-7}}{r^2}$ $[Tm^{-1}A^{-1}]$. Of course these results can also be found easily in the literature, for example in [20].

## 7.2 The Golay coil

Producing a transverse gradient field like the ones in $x$ and $y$ direction is a bit more complicated. Note that we cannot just use a rotated Maxwell pair as in this case we need the field gradient to be perpendicular to the field itself like the one shown in Figure 6.1.

The scheme of the Golay coil used to produce transverse gradients is shown in Figure 7.2. As can be seen this is also a cylindrical design made up of four identical saddles. The optimized parameters in this case are the axial distance of the two parts, the length of the curved parts in terms of the cylinder radius, and the total length of the coil. With calculations somewhat more complicated than in the case of the Maxwell pair one can show that the gradient linearity will reach its optimum if these parameters are set as written in Figure 7.2. The DSV of this design is about $1.2\,r$ and the efficiency is $\eta = \frac{9.2\times10^{-7}}{r^2}$ $[Tm^{-1}A^{-1}]$ as to be found in [20].

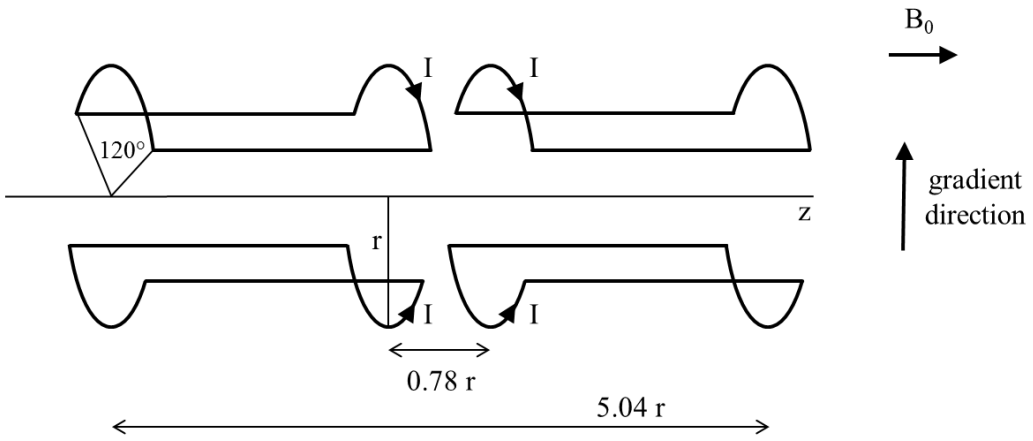


Figure 7.2: Golay design as a transverse ($x$ or $y$) gradient coil.

# 8. Construction and characterization of gradient coils

In this chapter I present the work with the built $z$ and $x$ gradient coils including the construction and the measurements of performance. For each coil we measured the resistance and the efficiency and also tested their homogeneity by performing 2D imaging experiment on a grid phantom.

## 8.1 Construction of gradient coils

As mentioned before, our $z$ and $x$ gradient coils were of the types Maxwell and Golay, respectively. Therefore during the design of the coils we only had one free parameter, the coil radius. The inner diameter of the NMR bore was 40 mm so we had to fit our probehead into this size. Therefore we decided the coils to have a medium diameter 35 mm. This is a medium diameter as both of the coils were made of foil insulated copper wire of a diameter 1 mm, so the inner and the outer diameter was 34 mm and 36 mm, respectively.

The coils are shown in Figure 8.1. Both of the coils are mounted on the same PVC tube, the left figure shows the state when the $x$ gradient coil was not built yet.

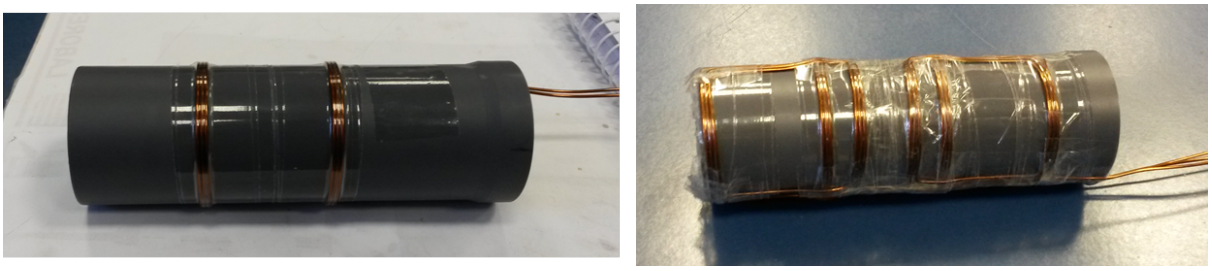

Figure 8.1: Left: $z$ gradient coil on PVC mount. Right: Both $x$ and $z$ gradient coils on the same mount.

The gradients were driven by two Delta power supplies of type ES 015-10 and ES 030-10 with a maximum available current 10 A. To get an estimation of the achievable gradient strength with this current limit we used the theoretical gradient efficiency of these designs mentioned in the previous chapter. The resulting values for our coils with the given radius:

$$\eta_x = 3.00 \left[\frac{mT}{Am \times turn}\right], \quad \eta_z = 2.63 \left[\frac{mT}{Am \times turn}\right] \tag{8.1}$$

Since we would like to achieve the typical gradient strength of 40-100 mT/m used in clinical devices we decided that both of our coil will consist 3 turns. In this way we could achieve approximately 90 mT/m with 10 A. However, the Maxwell and Golay designs were to describe coils with infinitely thin conductors, with 3 turns of a wire with a diameter 1 mm this condition will no longer be satisfied. We built both coils in a way that the middle turn was placed into the theoretical position of the conductors.

The approximate field of view (FOV) can also be calculated from the theory of the coils. Using the values given in the previous chapter our coils with the medium diameter of 35 mm will have a DSV of 17.5 mm for the $z$ gradient coil and 21 mm for the $x$ coil. Of course we had to ensure that the centres of the coils' field of views coincide in order to maximize the intersection of the two FOV-s. This condition is satisfied within a tolerance of 1 mm.

I note here that due to the lack of free space in the NMR bore the outer arcs of the $x$ gradient coil were built about 3 mm closer to the coil centre than the Golay design would say. Fortunately the $x$ gradient field is produced mainly by the inner arcs therefore such a small deviation of the optimal construction would hopefully not cause problems.

The PVC tube mounting the coils was fixed onto the probehead in a way that the RF coil is located inside the tube with the centre of the two coils coincide within a tolerance of 2 mm. The coil wires were equipped with banana plugs at the bottom of the probehead for power supply. The probehead with the gradient coils is shown in Figure 8.2.

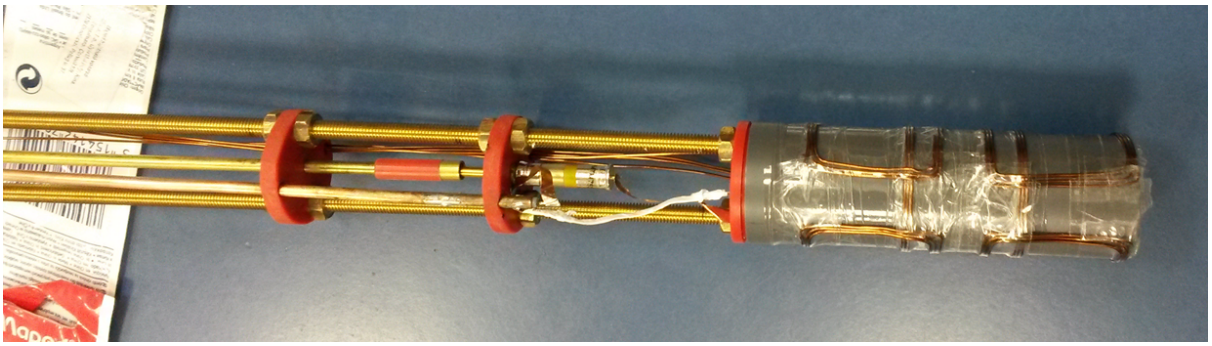

Figure 8.2: Probehead with $x$ and $z$ gradient coils and the RF coil inside.

## 8.2 Measurement of resistance

As previously mentioned the gradient coil current was provided by two Delta power supplies with adjustable voltage and current limits. Since the current in the gradient coils flows only during a time interval of milliseconds or even below that, we could not use the power supply's current display to measure the flowing current. We did not want to

use oscilloscopes all the time for this purpose so we had to measure the total resistance of the gradient coils and circuits. In this way we can calculate the current from the voltage display as the voltage is constant due to the switching circuit built by Gyula Gyebnár. The detailed description of the gradient driving system can be found in the Diploma Thesis of Gyula Gyebnár [12] as this was a part of his job in the project.

The scheme of the gradient control circuit and the ptoho of the two circuits are shown in Figure 8.3. The gradient switching was done by a FET controlled with a TTL signal from the spectrometer.

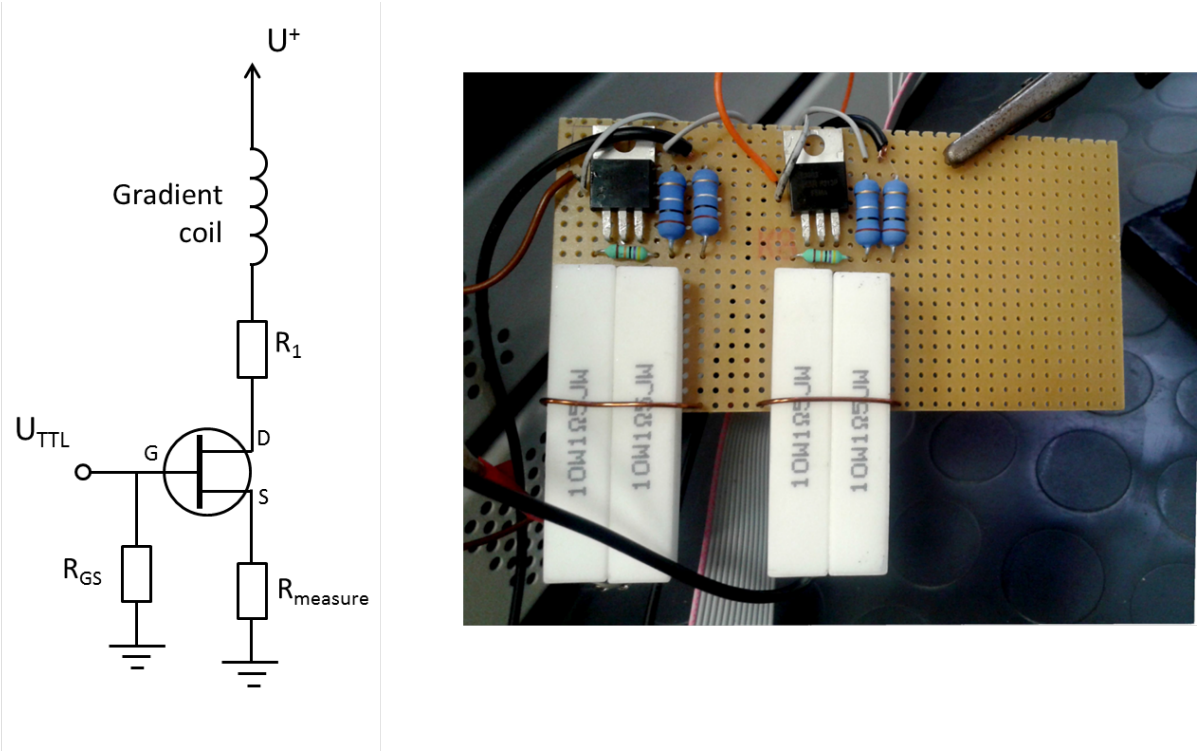


Figure 8.3: Left: scheme of the gradient control circuit. Right: Built gradient control circuits by Gyula Gyebnár.

We measured the resistance of the two gradient systems by applying various supply voltages to the circuits and measuring the voltage across the resistive element $R_{measure}$ of 50 mΩ from which the current can be calculated. This element is made up of two parallel resistances of 0.1 Ω, the blue ones in the above photo. Their voltage was measured with a Tektronix TDS 310 oscilloscope. During the voltage measurement we could also observe the gradient rise and fall times. One of the oscilloscope screens is shown in Figure 8.4. As can be seen the gradient swithing is quite fast with the value of approximately 10 µs, though there is an oscillation in the current when switching off.

We determined the resistance by fitting a linear curve to the voltage-current data points with fixed intersection at the origin. The result is shown in Figure 8.5.

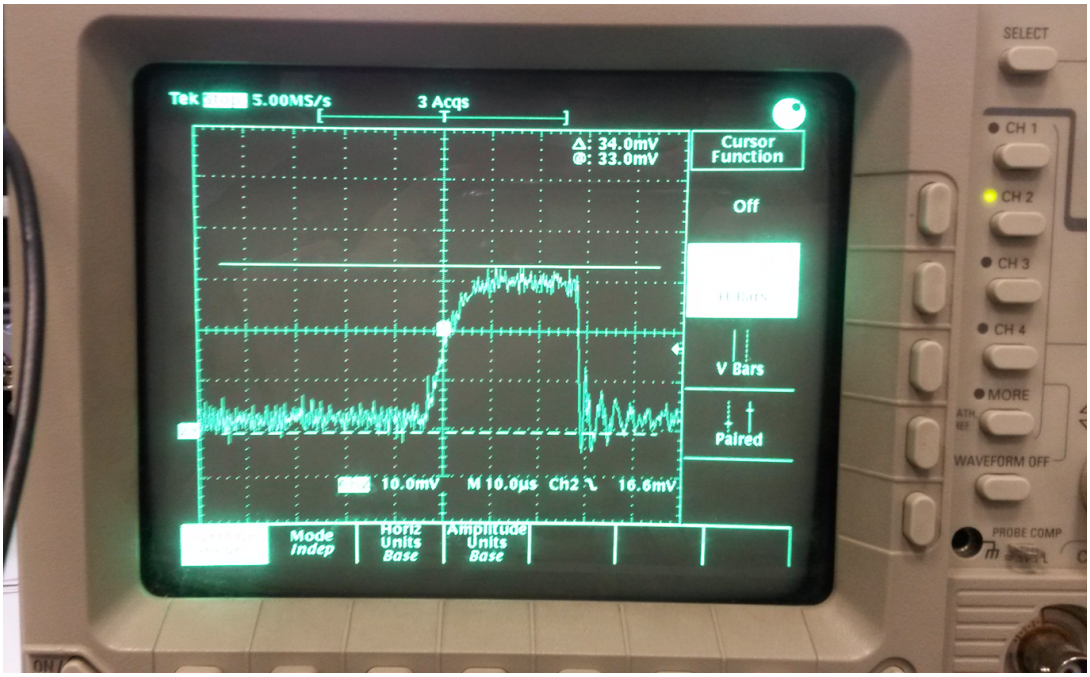


Figure 8.4: Gradient rise and fall times observed with oscilloscope on the measuring resistance.

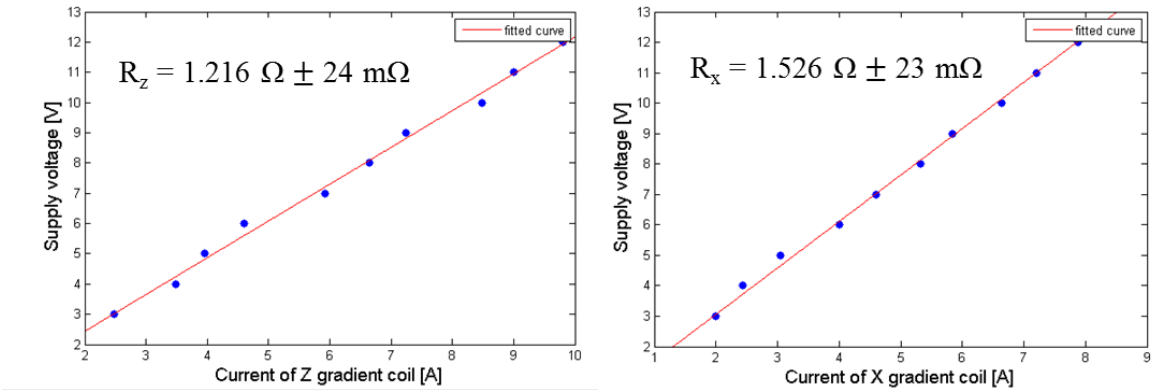


Figure 8.5: Supply voltage vs. gradient current, the fitted linear curves and the resulting resistances. Left: $z$ gradient, right: $x$ gradient.

## 8.3 Inspecting gradient efficiency

In order to use appropriate pulse sequences we had to know how strong gradient fields do our coils provide with a given current, that is, their actual gradient efficiency. We have measured this by acquiring 1D images of phantoms with known geometry and analyzing the results.

For the $z$ gradient coil we used a quartz tube with two water parts in it separated with a teflon plug as shown in Figure 8.6. We put this phantom into the proton coil with

Figure 8.6: Quartz tube with two water parts separated by a teflon plug; a phantom used for $z$ gradient efficiency measurement.

its geometric centre approximately to the coil centre and measured the FID sign with different currents flowing through the $z$ gradient coil. In this way the Fourier transform of the FID, i. e. the NMR spectrum will be the projection of the spin density onto the gradient direction, in other words, a 1D image of the sample. Therefore with a phantom shown in Figure 8.6 we achieved spectra with two distinct peaks associated to the two parts of water. As the gradient strength increases the distance between these peaks becomes larger (and of course their width as well) so the gradient efficiency can be obtained by measuring the peak distances on the spectra. The ratio of the frequency shift $\Delta f$ and the distance of the two water parts $\Delta x$ is proportional to the gradient strength $G$:

$$\Delta f = \frac{\Delta\omega}{2\pi} = \frac{\gamma}{2\pi} G\Delta x = \gamma G\Delta x \tag{8.2}$$

In Figure 8.7 one of the spectra acquired with $z$ gradient is shown as well as the peak distances as function of the applied gradient current with the fitted linear curve and the resulting gradient efficiency.

As can be seen the result is near to the theoretical efficiency of 7.89 mT/Am for our 3-turn coil from (8.1), the difference is about 8.2 %.

For the $x$ gradient coil we first tried to use the same method of measuring the peak distances. For this purpose we fabricated another phantom with two horisontally separated quartz tubes filled with water and planned to acquire images with $x$ gradient on. However when we tried to do the measurements we found that even without the application of

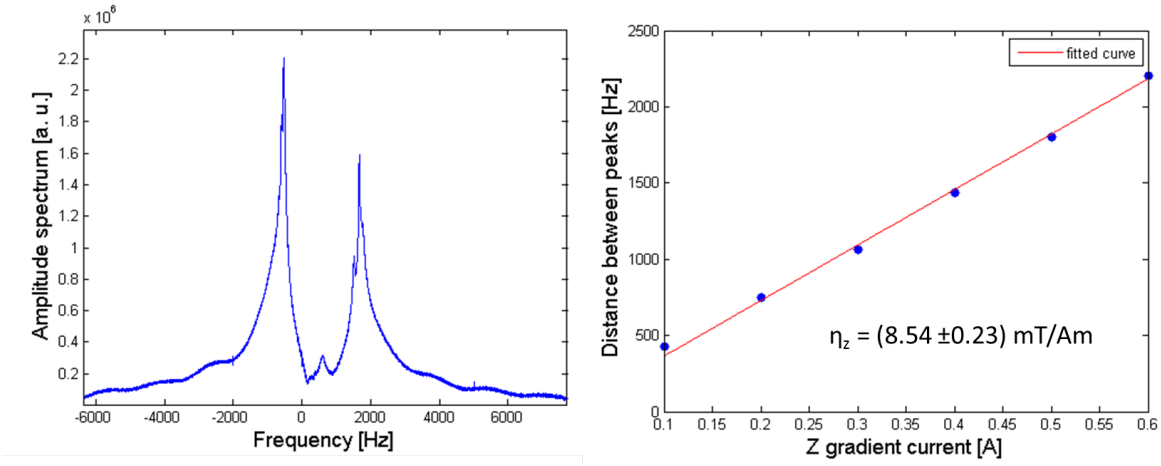


Figure 8.7: Left: Spectrum of phantom with 2 water parts with 0.6A current flowing through the $z$ gradient coil. Right: Peak distances vs. $z$ gradient current and the fitted linear curve with fixed intercept at the origin.

gradients the spectra were extremely wide and noisy due to main field inhomogeneities probably caused by the complicated structure of the phantom. We could not correct this inhomogeneity with the device's shimming coils that serve this purpose so this kind of experiments became impossible.

Figure 8.8: Cylindrical water phantom for $x$ gradient efficiency measurement. Left: Closed sample holder. Right: Opened sample holder with the water in it.

Because of this we decided to measure the $x$ gradient efficiency with another method. We put a cylindrical water sample shown in Figure 8.8 of height 10 mm and diameter 12 mm into the coil and measured the spectra with different gradient currents. With this sample the main field remained sufficiently homogeneous so this experiment could be carried out. The idea was that if we apply a gradient during the acquisition, i. e. measure the 1D image of the phantom the spectra will broaden due to the finite width of the

sample. This broadening will of course increase with the gradient currents and therefore suitable for measuring the gradient field strength.

In Figure 8.9 one of the spectra acquired with $x$ gradient is shown as well as the spectrum widths vs. the $x$ gradient current with the fitted linear curve with fixed intercept at the origin.

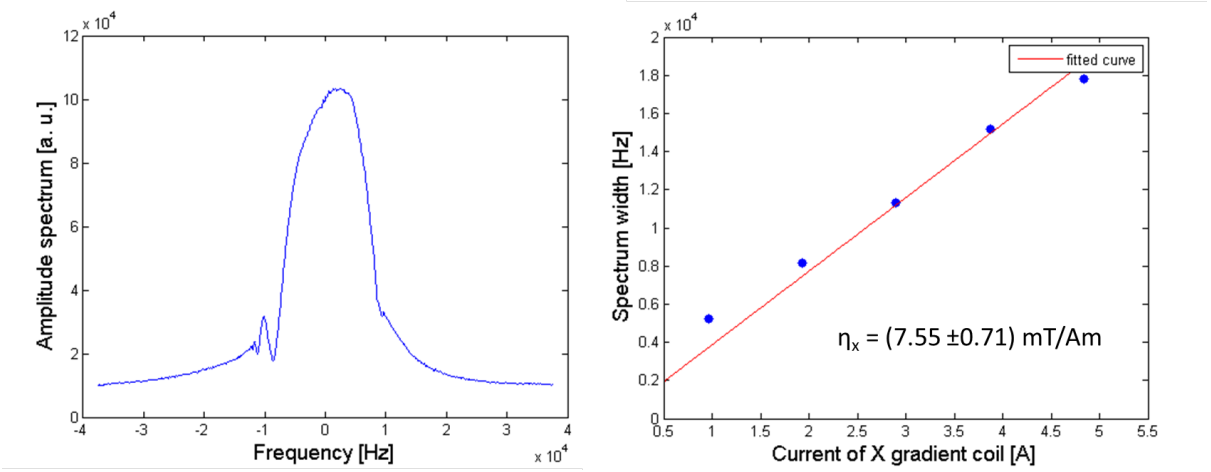


Figure 8.9: Left: Spectrum of cylindrical phantom with 5 A current flowing through the $x$ gradient coil. Right: Total spectrum width vs. $x$ gradient current and the fitted linear curve with fixed intercept at the origin.

In this case the real efficiency is found to be significantly lower than the theoretical value of 9 mT/mA, the difference is about 16.1 %. This deviation is either due to construction errors in the $x$ gradient coil or due to measurement inaccuracy as the linear curve does not fit too well onto the data points as can be seen in the large standard error.

However, a more accurate determination of the gradient strength can be done by 2D imaging of a sample with known geometry. We performed such measurement on the same cylindrical phantom shown in Figure 8.8 with an imaging sequence and reconstruction algorithm developed by Gyula Gyebnár. The detailed description of the imaging process can be found in Gyula's Diploma Thesis [12]. The idea is the following. We reconstruct the 2D image of the phantom with simple 2D inverse Fast Fourier Transform (FFT) thus getting the image with frequency scales in both directions. If we measure the extension of the sample in this image we can determine how broad was the frequency range produced by our gradient coil in the interval of the sample size. From this the gradient strength can be calculated easily using the formula (8.2).

The 2D image of the phantom is shown in Figure 8.10.

The size of the sample in this frequency scale was determined by the average width of the single-column and single-row slices of this 2D image, while the error of this result

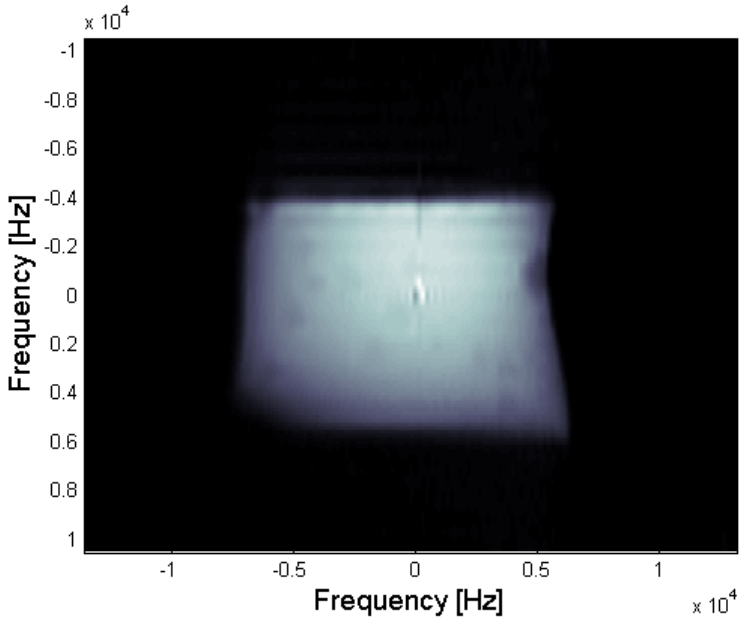


Figure 8.10: 2D image of the cylindrical phantom reconstructed by plain 2D FFT, with the frequency scales.

is descibed with the standard deviation of these widths. One of these slices is shown for both $x$ and $z$ directions in Figure 8.11.

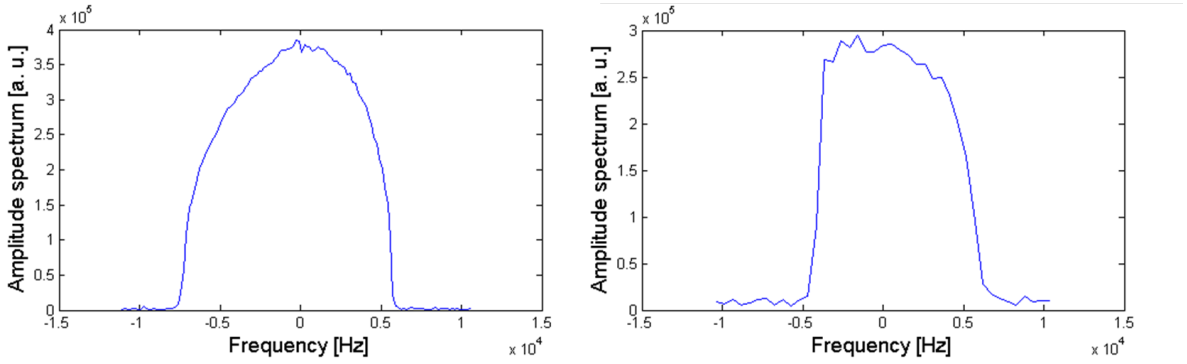


Figure 8.11: Left: Slice of the 2D image of the cylinder in $x$ direction. Right: Slice of the 2D image in $z$ direction.

The calculated gradient strengths are the followings:

$$\eta_x = 8.74 \pm 0.15 \frac{mT}{Am}, \quad \eta_z = 8.90 \pm 0.18 \frac{mT}{Am} \tag{8.3}$$

These results differ from the theoretical gradient efficiencies by 2.9 % ($x$) and 12.8 % ($z$). As can be seen these results have an error much smaller than the one acieved with the spectrum broadening measurement and therefore these values should be considered as the valid ones.

## 8.4 Gradient homogeneity testing with grid phantom

Finally we wanted to get some information about the gradient field homogeneities. An obvious method to do this is performing imaging experiments of phantoms with known geometry and analyzing the acquired images and their geometric distortion. The measurements were performed using the pulse sequences and reconstruction algorithm developed by Gyula Gyebnár. A detailed description of these can be found in Gyula's Thesis [12].

For this purpose we used a cylindrical Telfon cylinder with numerous mortises filled with water forming a grid as shown on the left in Figure 8.12. The diameter of the mortises is 2 mm while the lattice constant, i. e. the distance of the center of neighbouring holes is 4 mm. We performed a 2D experiment of this phantom in a plane where the mortises form a grid. The resulted image is shown on the right in Figure 8.12.

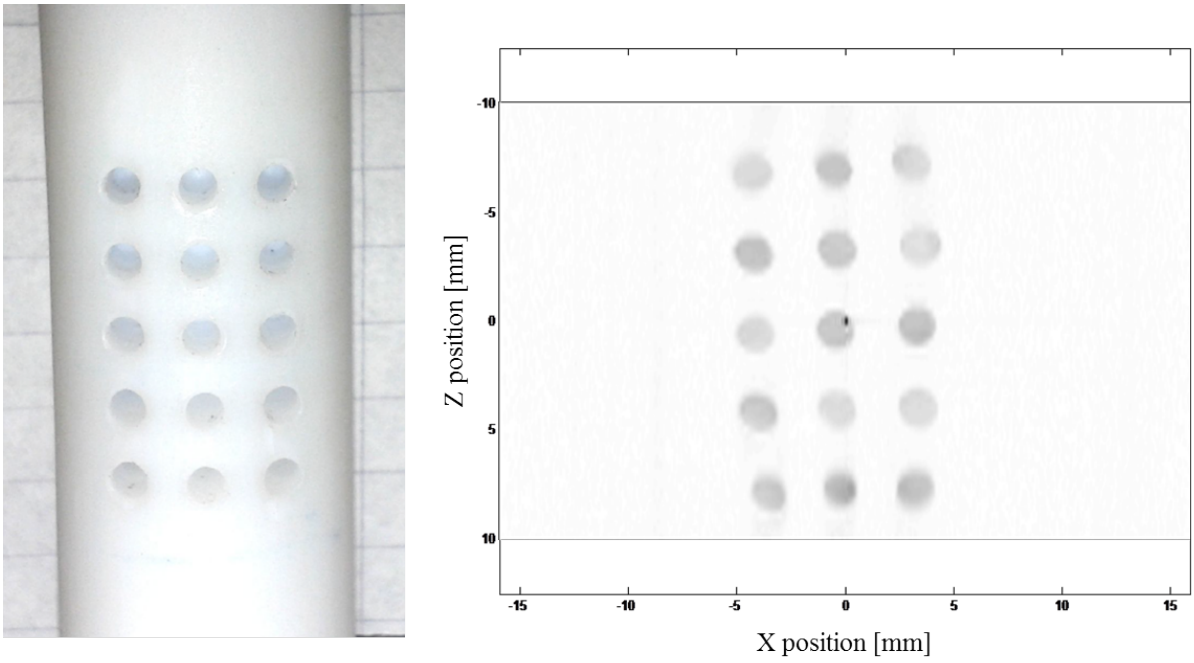


Figure 8.12: Left: Telfon cylinder with water-filled holes forming a grid. Right: Reconstructed 2D image of the phantom. Image inverted for better visibility.

As can be seen, geometric distortion is present in the edges of the image probably due to the fact that our phantom has a diameter of 20.6 mm measured along the diagonal which is greater than the DSV of the $z$ gradient coil and approximately the same as the DSV of the $x$ coil. The caused image distortions can be corrected with proper image processing, but the investigation of such a correction is beyond the limits of this thesis. However, images acquired of more complicated samples like cucumber of tomato slices show that even without such a correction we can achieve satisfying image quality. Some

of these images acuired with our probehead, pulse sequence and reconstruction algorithm are shown in the following figure.

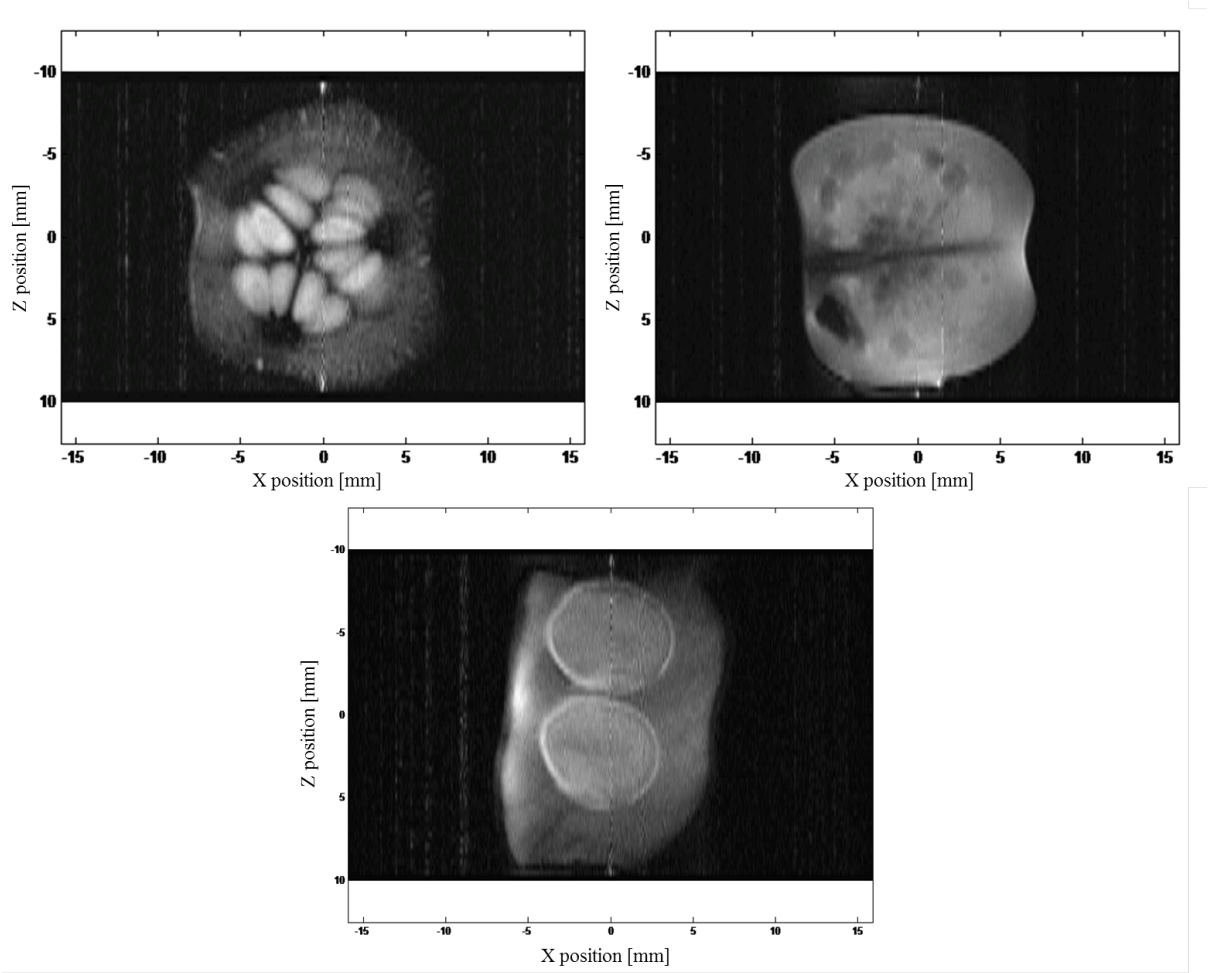


Figure 8.13: Images acquired with our probehead. Up left: Slice of cucumber. Up right: Slice of tomato. Down: Peapod with two peas in it.

# 9. Summary and conclusion

In this thesis work I aimed to build and characterize imaging probeheads for an NMR spectrometer operating at 7T. First I implemented a Matlab algorithm to predict the resonance frequencies of an unshielded Birdcage resonator with arbitrary geometry and used it to design my own coils for Sodium and Hydrogen nuclei. Thereafter I succesfully constructed the coils for these two nuclei and proved that their resonant behavior coincide very well with the predictions. After that I calibrated the needed pulse lengths for given excitation angles and verified that both coils provide sufficiently homogeneous transverse $B_1$ field.

Then I constructed two gradient coils of type Maxwell and Golay for our system and calculated their theoretical gradient efficiency and field of view. To drive the gradient coils with power supplies of given voltage I measured their resistance and showed that the gradient current can be switched in about 10 µs with the control circuit built by Gyula Gyebnár [12]. This switch rapidity allows the application of conventional MRI pulse sequences.

Thereafter I measured the gradient efficiency of the coils using different phantoms and methods and found it to be similar to the theoretical values of these designs. Gradient homogeneity was tested with a grid phantom; the measurement showed no significant inhomogenities (i. e. geometric distorsions) inside the field of view.

Performance of our probehead on actual samples was investigated by 2D imaging of various vegetables e.g. cucumber and tomato. Some of the acquired and reconstructed images are shown in the previous section. With our modified spin echo sequence we achieved the resolution of 320 µm in the phase encoding direction and 100 µm in the frequency encoding (readout) direction.

In the future we plan to upgrade this system with more state-of-art gradient coils and faster imaging sequences using the commercial gradient control and amplifier units recently received by the lab; as well as to develop time-dependent and spectroscopic imaging possibilities of Phosphorus in biologically relevant samples for pharmaceutical research purposes.

# A. Computation of mutual inductances in the Birdcage coil [19]

In this appendix the analytical calculations of mutual inductances in the Birdcage coil are presented as can be found in [19] as well as my code of numerical computation of these using Gauss quadrature for numeric integrals in Matlab environment.

Mutual inductance between two conductors $C_1$ and $C_2$ with current densities $\mathbf{J_1}$ and $\mathbf{J_2}$ with total currents of $I_1$ and $I_2$ is the following by definition [6]:

$$M = \frac{\mu_0}{4\pi I_1 I_2} \int_{C_1} \int_{C_2} \frac{\mathbf{J_1}(\mathbf{r})\mathbf{J_2}(\mathbf{r'})}{|\mathbf{r} - \mathbf{r'}|} \, \mathrm{d}^3\mathrm{r} \, \mathrm{d}^3\mathrm{r'} \tag{A.1}$$

If we apply this formula for the n-th and the k-th legs in an N-leg Birdcage coil with a radius R and assume that the strips are infinitely thin and the current is uniformly distributed along the strip width $\omega_b$ the mutual inductance will be:

$$L^b_{n,k} = \frac{\mu_0 R^2}{4\pi\omega_b^2} \int_0^h \int_{\theta_n}^{\theta_n+\omega_b/R} \int_0^h \int_{\theta_k}^{\theta_k+\omega_b/R} \frac{\mathrm{d}\theta \mathrm{d}z \mathrm{d}\theta' \mathrm{d}z'}{\sqrt{2R^2\left(1-\cos(\theta-\theta')\right)+(z-z')^2}} \tag{A.2}$$

where $h$ denotes the leg height and $\theta_k$ is the azimuthal angle of the k-th leg: $\theta_k = 2(k-1)\pi/N$.

By carrying out the integraton in $z$ and $z'$ the expression will become as follows:

$$\begin{aligned} L^b_{n,k} = \frac{\mu_0 R^2}{4\pi\omega_b^2} \int_{\theta_n}^{\theta_n+\omega_b/R} \int_{\theta_k}^{\theta_k+\omega_b/R} \Big[ & \sqrt{2R^2\left(1-\cos(\theta-\theta')\right)+h^2} \\ & + 2\sqrt{2R^2\left(1-\cos(\theta-\theta')\right)} + h\ln\left(h+\sqrt{2R^2\left(1-\cos(\theta-\theta')\right)+h^2}\right) \\ & - h\ln\left(-h+\sqrt{2R^2\left(1-\cos(\theta-\theta')\right)+h^2}\right)\Big] \mathrm{d}\theta \mathrm{d}\theta' \end{aligned} \tag{A.3}$$

With the same deduction the mutual inductances between the k-th and the n-th segments in the same endring are:

$$L^{a}_{n,k} = \frac{\mu_0 R^2}{4\pi\omega_a^2} \int_{2(n-1)\pi/N}^{2n\pi/N} \int_{2(k-1)\pi/N}^{2k\pi/N} \cos(\theta-\theta') \left[ 2\sqrt{2R^2(1-\cos(\theta-\theta'))} \right.$$
$$- 2\sqrt{2R^2(1-\cos(\theta-\theta')) + \omega_a^2} + \omega_a \ln\left(\omega_a + \sqrt{2R^2(1-\cos(\theta-\theta')) + \omega_a^2}\right)$$
$$\left. - \omega_a \ln\left(-\omega_a + \sqrt{2R^2(1-\cos(\theta-\theta')) + \omega_a^2}\right) \right] \mathrm{d}\theta \mathrm{d}\theta' \quad \text{(A.4)}$$

Where $\omega_a$ denotes the endring strip width. When the two chosen segments are in different endrigs the expression will be as follows:

$$L^{\bar{a}}_{n,k} = \frac{\mu_0 R^2}{4\pi\omega_a^2} \int_{2(n-1)\pi/N}^{2n\pi/N} \int_{2(k-1)\pi/N}^{2k\pi/N} \cos(\theta-\theta') \left[ 2\sqrt{2R^2(1-\cos(\theta-\theta')) + (L-\omega_a)} \right.$$
$$- \sqrt{2R^2(1-\cos(\theta-\theta')) + L^2} - \sqrt{2R^2(1-\cos(\theta-\theta')) + (L-2\omega_a)^2}$$
$$- 2(L-\omega_a) \ln\left(L - \omega_a + \sqrt{2R^2(1-\cos(\theta-\theta')) + (L-\omega_a)^2}\right)$$
$$+ L \ln\left(L + \sqrt{2R^2(1-\cos(\theta-\theta')) + L^2}\right)$$
$$\left. - (L-2\omega_a) \ln\left(L - 2\omega_a + \sqrt{2R^2(1-\cos(\theta-\theta')) + (L-2\omega_a)^2}\right) \right] \mathrm{d}\theta \mathrm{d}\theta' \quad \text{(A.5)}$$

Where L is the total height of the coil. From these inductance values the elements of the magnetic coupling matrix, i. e. the mutual inductances of the meshes can be derived easily:

$$M_{n,k} = L^{b}_{n,k} - L^{b}_{n+1,k} - L^{b}_{n,k+1} + L^{b}_{n+1,k+1} + 2\left(L^{a}_{n,k} - L^{\bar{a}}_{n,k}\right) \quad \text{(A.6)}$$

Because of the circulant property of the magnetic coupling matrix we only need the first row of the matrix $\mathbf{M}$, i. e. the elements $M_{n,k}$ where $n = 1$. From the above equation it can be seen that for this we only need $n = 1$ elements from the endring inductances matrix and $n = 1, 2$ elements from the leg inductances matrix. In the numerical algorithm only these elements are calculated as shown in my following Matlab codes.

For the calculation of leg inductances:

```
function y = Mleg(theta1,theta2,R,h)
kicsi=eps;
y = -2*sqrt(2*R^2*(1-cos(theta1-theta2))+h^2)...
+ 2*sqrt(2*R^2*(1-cos(theta1-theta2)))...
+ h*log(kicsi+h+sqrt(2*R^2*(1-cos(theta1-theta2))+h^2))...
```

```
- h*log(kicsi-h+sqrt(2*R^2*(1-cos(theta1-theta2))+h^2));
end

function [Lb] = Mleg_int(R,h,wb,N)
%Calculates the inductive couplings from
%geometrical parameters using Gauss quadrature.
Lb=zeros(N);
for k=1:N
for n=1:2
theta_n=2*(n-1)*pi/N;
theta_k=2*(k-1)*pi/N;
Lb(n,k)=10^-7*R^2/(wb^2)*dblquad(@(theta1,theta2)...
Mleg(theta1,theta2,R,h),theta_n,theta_n+wb/R,theta_k,theta_k+wb/R);
end
end
end
```

For the calculation of endring inductances:

```
function y = Marc(theta1,theta2,R,Z,wa)
kicsi=eps;
y=cos(theta1-theta2).*(...
2*sqrt(2*R^2*(1-cos(theta1-theta2))+Z^2)...
-sqrt(2*R^2*(1-cos(theta1-theta2))+(Z+wa)^2)...
-sqrt(2*R^2*(1-cos(theta1-theta2))+(Z-wa)^2)...
-2*Z*log(kicsi+Z+sqrt(2*R^2*(1-cos(theta1-theta2))+Z^2))...
+(Z+wa)*log(kicsi+Z+wa+sqrt(2*R^2*(1-cos(theta1-theta2))+(Z+wa)^2))...
+(Z-wa)*log(kicsi+Z-wa+sqrt(2*R^2*(1-cos(theta1-theta2))+(Z-wa)^2)));
end

function [La1,La2] = Marc_int(R,wa,N,H)
%Calculates the inductive couplings from
%geometrical parameters using Gauss quadrature.
La1=zeros(N);
La2=zeros(N);
n=1;
for k=1:N
Z=0;
La1(n,k)=10^-7*R^2/(wa^2)*dblquad(@(theta1,theta2)...
```

```
Marc(theta1,theta2,R,Z,wa),2*(n-1)*pi/N,2*n*pi/N,2*(k-1)*pi/N,2*k*pi/N);
Z=H-wa;
La2(n,k)=10^-7*R^2/(wa^2)*dblquad(@(theta1,theta2)...
Marc(theta1,theta2,R,Z,wa),2*(n-1)*pi/N,2*n*pi/N,2*(k-1)*pi/N,2*k*pi/N);
end
```

From these values the magnetic couplings are computed as follows:

```
function [ L ] = indukc( R,wa,wb,N,H,h )
%Calculates the elements of the magnetic coupling matrix
%from the leg and endring inductances.
[ Lb ] = Mleg_int( R,h,wb,N );
[ La1,La2 ] = Marc_int( R,wa,N,H );
L=zeros(N);
for k=1:N
for n=1:1
L(n,k)=2*Lb(n,k)-Lb(mod(n,N)+1,k)-Lb(n,mod(k,N)+1)+2*(La1(n,k)-La2(n,k));
end
end
```

The resonance frequencies of the Birdcage coil are calculated using the following function:

```
function [ w ] = birdcage( Ca,Cb,D,wa,wb,N,H )
%Calculates the resonant frequencies of the Birdcage coil
%from its geometrical parameters. Ca and Cb are the capacitances
%of the endring and leg capacitors in pF, D is the diameter
%of the coil, H is the total height of the coil, wa and wb
%are the endring and leg widths, N i %the number of legs.
h=H-2*wa;
R=D/2;
L=indukc(R,wa,wb,N,H,h);
L1=L(1,:);
N=max(size(L1));
Ca=Ca*1E-12;
Cb=Cb*1E-12;
M=fft(L1)';
j=linspace(0,N-1,N)';
w=sqrt((2./M).*(1/Ca+(1/Cb).*(1-cos(2*j*pi/N))));
```

```
f=w/(2*pi)*1E-6;
%this is the resonant frequency vector in MHz.
end
```

# B. Precession at static magnetic field - quantum mechanical description

In quantum mechanics both angular and magnetic moment are represented by hermitic operators characterized by their eigenvalues and eigenstates. For the square of the angular momentum, $J^2$ the possible eigenvalues are

$$J^2 = \hbar^2 I(I+1) \tag{B.1}$$

Where I is the integer or half-integer quantum number of the angular momentum. For the projection of the angular momentum to a specific directon, for example to $\mathbf{e_z}$:

$$J_z = \hbar m, \qquad -I \leq m \leq I \tag{B.2}$$

For a single spin-half particle, there is a similar relation between angular and magnetic moment as it was in the classical case, that is

$$\boldsymbol{\mu} = \gamma \mathbf{J} \tag{B.3}$$

Therefore the matrix elements of a specific component of the magnetic moment can be computed using the angular momentum operator. With the bra-ket notation introduced by Dirac, the matrix element with the states described by quantum numbers (I, m) and (I, m'):

$$\langle I, m | \mu_x | I, m' \rangle = \gamma \langle I, m | J_x | I, m' \rangle \tag{B.4}$$

If the particle is placed into external magnetic field, its originally degenerated spectrum splits based on the projection of the magnetic moment to the external field - this is called the Zeeman effect. The descriptive Hamiltonian:

$$H_{Zeeman} = -\gamma \hbar \mathbf{JB} \tag{B.5}$$

If the external magnetic fields is $B_0$ then the splitted energy levels are

$$E_m = -\gamma \hbar B_0 m = -\hbar m \omega_0 \tag{B.6}$$

In general, the wavefunction of the particle is a sum of the eigenstates with different weights, each multiplied by the time propagation term with one of the energies described above

$$\Psi(t) = \sum_{m=-I}^{I} C_m \big| I, m \big\rangle \mathrm{e}^{-\frac{\mathrm{i}}{\hbar} E_m t} \tag{B.7}$$

Using equations (B.4) and (B.7) we can compute the mean value of $\mu_x$ for a spin-half particle, exploiting the fact that in this case $I = \frac{1}{2}$.

$$\big\langle \mu_x \big\rangle = \big\langle \Psi(t) \big| \mu_x \big| \Psi(t) \big\rangle = V \sum_{m,m'} \gamma\hbar C^*_{m'} C_m \big\langle m' \big| J_x \big| m \big\rangle \mathrm{e}^{\frac{\mathrm{i}}{\hbar}\left(E_{m'} - E_m\right)t} \tag{B.8}$$

Now we express the $x$ component of the angular momentum with the usual ladder operators

$$J^+ = J_x + \mathrm{i} J_y \tag{B.9a}$$

$$J^- = J_x - \mathrm{i} J_y \tag{B.9b}$$

$$J^+ \big| I, m \big\rangle = \sqrt{I(I+1) - m(m+1)} \big| I, m+1 \big\rangle \tag{B.10a}$$

$$J^- \big| I, m \big\rangle = \sqrt{I(I+1) - m(m-1)} \big| I, m-1 \big\rangle \tag{B.10b}$$

$$J_x = \frac{1}{2}\Big( J^+ + J^- \Big) \tag{B.11a}$$

$$J_y = \frac{1}{2\mathrm{i}}\Big( J^+ - J^- \Big) \tag{B.11b}$$

After that substitute (B.6), (B.11a) and (B.10) in (B.8), consider the fact that both $m$ and $m'$ can only take the values of $\frac{1}{2}$ and $-\frac{1}{2}$, and that eigenstates with different $m$ values are orthogonal to each other:

$$\big\langle \mu_x \big\rangle = \frac{1}{2} V\gamma\hbar \left( C^*_{\frac{1}{2}} C_{-\frac{1}{2}} \mathrm{e}^{-\mathrm{i}\omega_0 t} + C_{\frac{1}{2}} C^*_{-\frac{1}{2}} \mathrm{e}^{\mathrm{i}\omega_0 t} \right) = V\gamma\hbar\, \Re\left( C^*_{\frac{1}{2}} C_{-\frac{1}{2}} \mathrm{e}^{-\mathrm{i}\omega_0 t} \right) \tag{B.12}$$

Without loss of generality we can assume that $C_{\frac{1}{2}} = a\mathrm{e}^{\mathrm{i}\alpha}$ and $C_{-\frac{1}{2}} = b\mathrm{e}^{\mathrm{i}\beta}$ for some $a, b, \alpha, \beta$ real numbers. Furthermore, the normalization criterion requires that $|C_{\frac{1}{2}}|^2 + |C_{-\frac{1}{2}}|^2 = \frac{1}{V}$, which allowes us to write $a$ and $b$ as $a = \frac{1}{\sqrt{V}}\cos\big(\frac{\theta}{2}\big)$ and $b = \frac{1}{\sqrt{V}}\sin\big(\frac{\theta}{2}\big)$. Using these expressions (B.13) becomes the following:

$$\big\langle \mu_x \big\rangle = V\gamma\hbar ab \cos\big(\alpha - \beta + \omega_0 t\big) = \frac{\gamma\hbar}{2}\sin(\theta)\cos\big(\alpha - \beta - \omega_0 t\big) \tag{B.13}$$

In an absolutely similar manner one can show that the mean values of the other two components of magnetic moment will be the following:

$$\langle \mu_x \rangle = \frac{\gamma\hbar}{2}\sin(\theta)\sin\big(\alpha - \beta - \omega_0 t\big) \tag{B.14}$$

$$\langle \mu_x \rangle = \frac{\gamma\hbar}{2}\cos(\theta) \tag{B.15}$$

With these expressions we have presented that the quantum mechanical calculations of a spin-half particle also shows the precession movement in the sense of mean values as equations (B.13), (B.14) and (B.15) describe a vector that precesses around axis $z$ with angular frequency $\omega_0 = -\gamma B_0$.

# Bibliography


[1] W. Gerlach and O. Stern: Ueber die Richtungsquantelung im Magnetfeld. *Ann. Phys., 74: 673, 1924*

[2] I. I. Rabi, J. R. Zacharias, S. Millman and P. Kusch: A new method of measuring nuclear magnetic moments. *Phys. Rev., 53: 318, 1938*

[3] E. M. Purcell, H. C. Torrey and R. V. Pound: Resonance absorption by nuclear magnetic moments in a solid. *Phys. Rev., 69: 37, 1946*

[4] F. Bloch: Nuclear induction. *Phys. Rev., 70: 460, 1946*

[5] E. L. Hahn: Spin Echoes. *Phys. Rev., 80: 580, 1950*

[6] E. Mark Haacke, Robert W. Brown, Michael R. Thompson and Ramesh Venkatesan: Magnetic Resonance Imaging: physical principles and sequence design. *ISBN 0-471-35128-8, [DNLM: 1. Magnetic Resonance Imaging. 2. Physics. WN 185 M1965, 1999] RC78.7.N83M3473 1999, 616.07'548-dc21, DNLM/DLC, for Library of Congress, 99-22880 CIP*

[7] J. D. Jackson: Classical Electrodynamics. *New York, NY: Wiley, ISBN: 9780471309321*

[8] I. I. Rabi, N. F. Ramsey and J. Schwinger: Rotating coordinates in magnetic resonance problems. *Rev. of Modern Phys., 26: 167, 1954*

[9] N. Bloembergen, E. M. Purcell and R. V. Pound: Relacation effects in nuclear magnetic resonance experiments. *Phys. Rev., 73: 679, 1948*

[10] D. I. Hoult and R. E. Richards: The signal-to-noise ratio of the nuclear magnetic resonance experiment. *J. Magn. Reson., 24: 71, 1976*

[11] Figure by Gavin W. Morley: SpinEcho_GWM_stills.jpg, licensed under the Creative Commons Attribution-Share Alike 3.0 Unported license. The copyright holder is Gavin W. Morley, I do not own any rights. link: `http://en.wikipedia.org/wiki/File:SpinEcho_GWM_stills.jpg`

[12] Gyula Gyebnár: 7T Bruker NMR mágneshez épített MRI mérőfej jelfeldolgozása és képalkotása, *Master Thesis, Budapest University of Technology and Economics, 2014*

[13] D. I. Hoult, R. Deslauriers, *Mag. Reson. Med. 16 (1990) 411.*

[14] S. M. Ould Ahmed Ghaly, L. Guendouz, A. Hedjiedj, .J. M. Escanyé, D. Canet, in: C. Ruggiero (Ed.), *Biomedical Engineering, vol. 519, 2006, p. 117*

[15] D. I. Hoult and R. E. Richards, *J. Magn. Reson. 24, 71, 1976*

[16] D. W. Alderman, D. M. Grant, *J. Magn. Reson. 36 (1979) 447.*

[17] C. E. Hayes, William A. Edelstein, John F. Schenck, Otward M. Mueller, and Matthew Eash: An efficient, highly homogeneous radiofrequency coil for whole-body NMR imaging at 1.5 T *J. Magn. Reson. 63, 622-628 (1985)*

[18] Mark C. Leifer: Resonant Modes of the Birdcage Coil. *J. Magn. Reson. 124, 51-60 (1997)*

[19] P. Boissoles and G. Caloz: Accurate calculation of mutual inductance and magnetic fields in a birdcage coil. *Preprint 06-07, Universite de Rennes 1, 2006*

[20] Clemente Cobos Sánchez: Forward and inverse analysis of electromagnetic fields for MRI using computational techniques. *PhD Thesis, The University of Nottingham, 2008*

[21] Chih-Liang Chin, Christopher M. Collins, Shizhe Li, Bernard J. Dardzinski and Michael B. Smith: BirdcageBuilder: Design of specified-geometry birdcage coils with desired current pattern and resonant frequency. *Concepts in Magnetic Resonance, Volume 15, Issue 2, pages 156-163, June 2002*

[22] Datasheet of the used SMD coils.
220 pF: `http://capacitoredge.kemet.com/capedge2/DataSheet/Datasheet-C1206C221K5RAC7867.pdf?pn=C1206C221K5RAC7867`,
22 pF: `http://capacitoredge.kemet.com/capedge2/DataSheet/Datasheet-C1206C220K5RAC7867.pdf?pn=C1206C220K5RAC7867`,
18 pF: `http://capacitoredge.kemet.com/capedge2/DataSheet/Datasheet-C1206C180K5RAC7867.pdf?pn=C1206C180K5RAC7867`

[23] Anita Karsa, Ferenc Simon: Magmágneses rezonancia laborgyakorlat. *Giude to practical course, Budapest University of Technology and Economics, 2012*

[24] I. I. Rabi: Space Quantization in a Gyrating Magnetic Field. *Phys. Rev. 51: 652, 1937*

[25] Sampo Mattila: Measurement and minimization of field inhomogeneities in high resolution NMR *Academic Dissertation, University of Oulu, 2001*

[26] István Faragó, Róbert Horváth: Numerikus módszerek *Typotex, 2013*